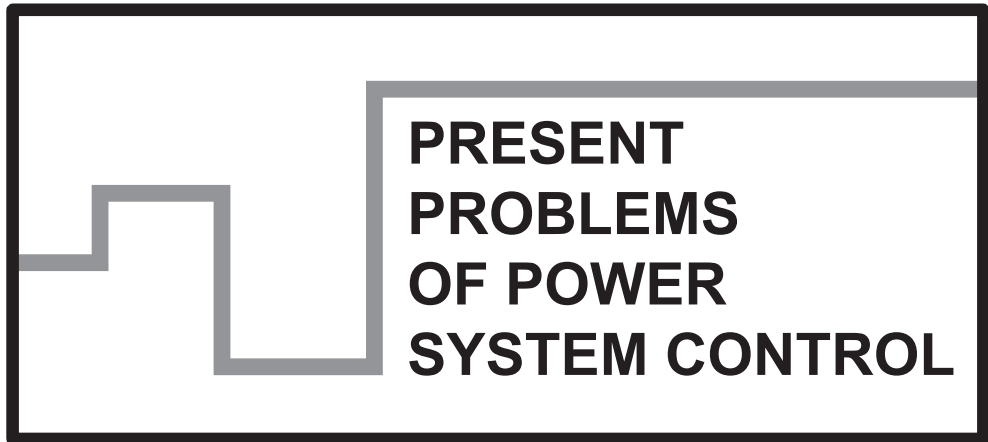


**Scientific Papers of  
the Department of Electrical Power Engineering of  
the Wrocław University of Science and Technology**



**Wrocław 2018**

## Guest Reviewers

Ivan DUDURYCH  
Tahir LAZIMOV  
Murari M. SAHA

## Editorial Board

Piotr PIERZ – art manager  
Mirosław ŁUKOWICZ, Jan IŻYKOWSKI, Eugeniusz ROSOŁOWSKI,  
Janusz SZAFRAN, Waldemar REBIZANT, Daniel BEJMERT

## Cover design

Piotr PIERZ

Printed in the camera ready form

Department of Electrical Power Engineering  
Wrocław University of Science and Technology  
Wybrzeże Wyspiańskiego 27, 50-370 Wrocław, Poland  
phone: +48 71 320 35 41  
www: <http://www.weny.pwr.edu.pl/instytuty,52.dhtml>; <http://www.psc.pwr.edu.pl>  
e-mail: [wydz.elektryczny@pwr.edu.pl](mailto:wydz.elektryczny@pwr.edu.pl)

All right reserved. No part of this book may be reproduced by any means, electronic, photocopying or otherwise, without the prior permission in writing of the Publisher.

© Copyright by Oficyna Wydawnicza Politechniki Wrocławskiej, Wrocław 2018

OFICyna WYDAWNICZA POLITECHNIKI WROCLAWSKIEJ  
Wybrzeże Wyspiańskiego 27, 50-370 Wrocław  
<http://www.oficyna.pwr.edu.pl>  
e-mail: [oficwyd@pwr.edu.pl](mailto:oficwyd@pwr.edu.pl)  
[zamawianie.ksiazek@pwr.edu.pl](mailto:zamawianie.ksiazek@pwr.edu.pl)

ISSN 2084-2201

Print and binding: beta-druk, [www.betadruk.pl](http://www.betadruk.pl)

## CONTENTS

Yu. KOZHUSHKO, T. KARBIVSKA, D. ZINCHENKO, D. PAVKOVIĆ, E. ROSOŁOWSKI, O. BONDARENKO, Charging Device of Capacitive Energy Storage for Micro Resistance Welding .....	5
B. KASZTENNY, A. GUZMÁN, M. V. MYNAM, T. JOSHI, Controlling Autoreclosing on Overhead Lines with Underground Cable Sections Using Traveling-Wave Fault Location Based on Measurements from Line Terminals Only .....	19
K. KLEN, V. ZHUIKOV, Approximation and Prediction of the Wind Speed Change Function .....	35
J. SZAFRAN, E. ROSOŁOWSKI, Dynamically Corrected Fast Estimators of Active and Reactive Power and Their Performance .....	47



*micro resistance welding, supercapacitor,  
capacitive energy storage, flyback converter*

Yuliia KOZHUSHKO\*, Tetiana KARBIVSKA\*,  
Denys ZINCHENKO\*\*\*, Danijel PAVKOVIC\*\*\*,  
Eugeniusz ROSOŁOWSKI\*\*\*\*, Oleksandr BONDARENKO\*

## **CHARGING DEVICE OF CAPACITIVE ENERGY STORAGE FOR MICRO RESISTANCE WELDING**

Micro resistance welding is the most common technology for making permanent connection between two conducting materials. This paper proposes a high-efficiency charging device for the capacitive energy storage within the micro resistance welding device power supply utilizing a Flyback converter. Based on the comprehensive analysis of charging device losses, it is determined that one of the main sources of conduction losses in the charging device is the output diode. In order to ameliorate this problem, utilization of a MOSFET transistor as an output diode within the Flyback converter is proposed in order to increase its overall efficiency. The presented results suggest that the proposed Flyback converter topology could improve the power efficiency by 7.0% at 50 kHz switching frequency through minimization of conduction losses in comparison with the traditionally-used Schottky diode.

### **1. INTRODUCTION**

Micro resistance welding is one of the most effective welding technologies widely used by the electronics industry today. Micro resistance welding is performed between two pieces of conducting material by means of resistive heating caused by the passage of high-magnitude electric current [1].

The current amplitude for micro resistance welding typically ranges from hundreds to thousands of amperes and depends on material type and thicknesses of individual parts. Energy consumption of significant power and short duration followed by long pauses between each pulsed welding discharge are load features of the micro resistance welding device. These features determine the negative impact of welding equipment on

---

\* National Technical University of Ukraine "Igor Sikorsky Kyiv Polytechnic Institute", Kyiv, Ukraine.

\*\* Tallinn University of Technology, Tallinn, Estonia.

\*\*\* University of Zagreb, Zagreb, Croatia.

\*\*\*\* Wrocław University of Science and Technology, Wrocław, Poland

the utility electrical grid in terms of high-magnitude pulsed loads and voltage drops at the point of grid connection, and possible harmonic distortion of the grid voltage if switched AC power supply is used. One of the effective methods for mitigating of this problem is using suitable Energy Storage topology within the power supply for the welding equipment. The operation of such power supplies can be based on the capacitive energy storage, which can provide fast energy discharge required for the welding process during the required time interval [2]. Moreover, during charging of the capacitive energy storage, energy is consumed from the grid evenly, almost without a negative influence on it. Capacitive energy storage of the power supply has to accumulate enough energy to provide hundreds of thousands of charge/discharge cycles and ensure fast and efficient energy transfer to the load [2].

Due to the high energy density, Li-ion battery is commonly applied as energy storage in mobile devices. However, the high-amplitude pulsed load, which is inherent to the welding equipment, drastically degrades the operational characteristics and the useful cycle life and calendar life of the Li-ion battery [3]. An effective solution for micro resistance welding power supply is using supercapacitors. Due to high capacity, low leakage current, thermal characteristics, shelf life, supercapacitors could be used as capacitive energy storage of power supply for micro resistance welding [4].

Charging devices for capacitive energy storage have to provide significant current and low terminal voltage, because of peculiarities of the load. Moreover, energy efficiency and parameters of weight and size are the key parameters in the design of charging devices. Small size and weight could be achieved due to the increase in the switching frequency. However, the increase of the switching frequency causes a rise in the dynamic power losses. Conduction losses of the low-power converter are dependent on the current passing through the semiconductor components and they significantly reduce efficiency. Thus, choice of the optimal converter topology and thorough losses analysis are key points for the design of high-efficiency charging device [5].

Designing supercapacitor charging devices is an specific problem, which is discussed by a number of authors. For example, [5], [6] propose a supercapacitor charging device using a soft-switching full-bridge pulse-width modulated (PWM) converter. The proposed converter has the advantages of lower switch voltage stresses and reduced circulating current. A buck dc-dc converter is presented in reference [7] and used for supercapacitor charging. This paper describes the converter circuit by using a system of differential equations, and shows that the converter is capable of stable operation subject to different distortion sources. Reference [8] presents the converter for supercapacitor charging, that uses a resonant inverter, which can start its operation directly in steady mode, hereof can work in a mode close to short-circuit at the load side. It should be noted, however, that the authors of these papers do not consider the peculiarities of the load characteristic of the micro resistance welding process.

Thus, the aim of the work is to improve the circuit topology of the charging device for the capacitive energy storage of power supply for micro resistance welding.

## 2. CHARGING DEVICE FOR THE CAPACITIVE ENERGY STORAGE OF POWER SUPPLY FOR MICRO RESISTANCE WELDING

The developed circuit topology of the power supply for welding Multicell Pulse Generator is represented in Fig. 1.

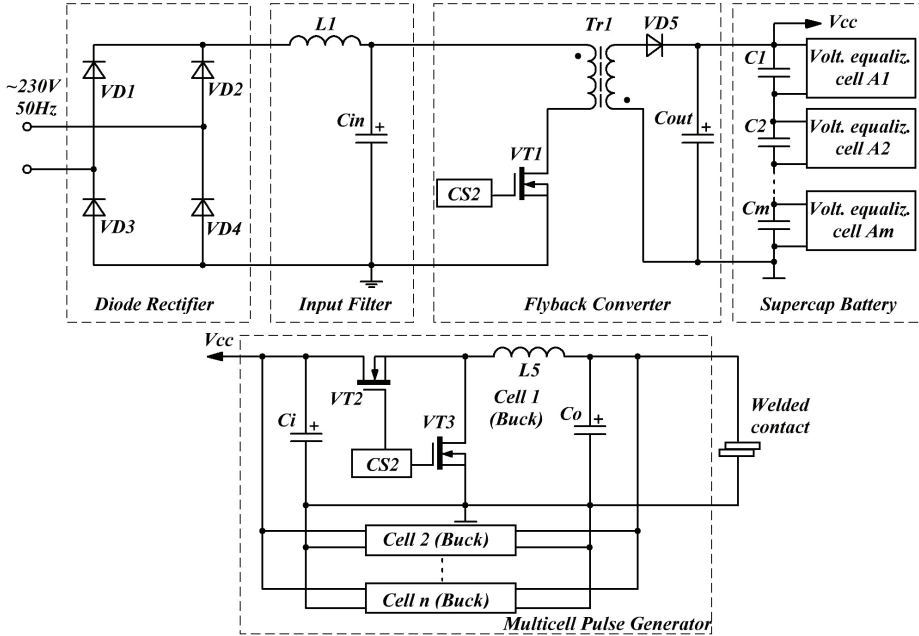


Fig. 1. Topology of power supply for micro resistance welding

This topology includes the following units. The Diode Rectifier rectifies the grid AC voltage with the frequency of 50 Hz, whereas the Input Filter smooths the rectified (pulsed) DC voltage characterized by significant 100 Hz ripple. The Flyback Converter provides the voltage for charging the supercapacitor module. Multicell Pulse Generator regulates the welding current in the load. The Buck dc-dc converter topology is chosen as the basis for converter cells control under welding conditions.

The power supply is, in fact, a charger for the energy storage – the Supercap Battery, which includes  $m$  supercapacitors (350 F each) connected in series

The load of the circuit is the Supercap Battery. In this specific case, the main criteria for the choice of supercapacitor type are not a capacitance but an equivalent series resistance (ESR), which should be as small as possible. The analysis showed that the decrease of supercapacitor ESR is typically accompanied by the increase of its capacitance, and vice versa. The energy efficiency of the supercapacitor battery during discharge is defined by the following equation [9]:

$$\eta_c = \frac{W_U - W_{loss}}{W_U}, \quad (1)$$

where  $W_{loss}$  is the energy dissipated on the supercapacitor equivalent series resistors, and  $W_U$  is the usable energy within the supercapacitor, given by:

$$W_U = \frac{1}{2}CU_{max}^2 - \frac{1}{2}CU_{min}^2, \quad (2)$$

where  $U_{max}$  denotes the rated supercapacitor voltage and  $U_{min}$  represents the minimum allowed supercapacitor voltage once the discharge is finished.

Figure 2 shows the efficiency dependence on the discharging current for the supercapacitor cells whose parameters are listed in Table 1. Energy losses on the equivalent series resistors during the discharge of the supercapacitor are given by:

$$W_{loss} = R_{ESR}i_{disch}^2t_{disch}, \quad (3)$$

where  $i_{disch}$  is the discharge current of the supercapacitor battery,  $R_{ESR}$  is the equivalent series resistance and  $t_{disch}$  is the discharging time.

Table 1. Parameters of supercapacitor cells from different manufacturers

Manufacturer	Rated voltage	Rated capacitance	Maximum ESR
Maxwell	2.7 V	350 F	3.2 mΩ
Nesscap	2.7 V	360 F	2.9 mΩ
Samwha	2.7 V	360 F	3.8 mΩ

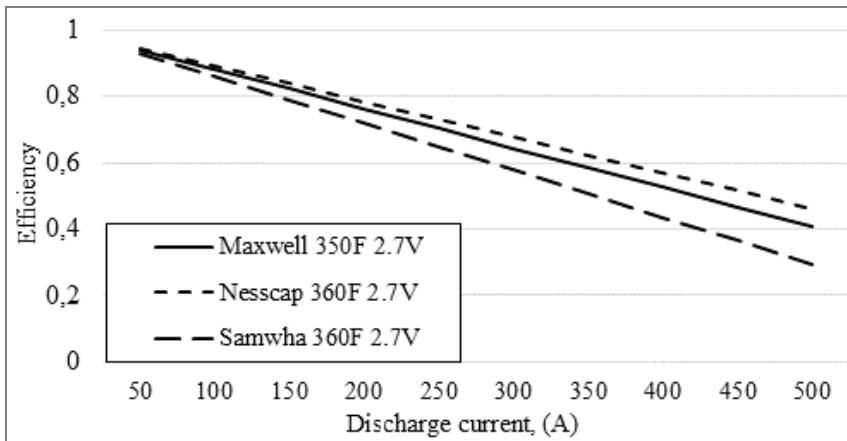


Fig. 2. Efficiency vs. discharging current bar graphs for different supercapacitor batteries

So, the choice of supercapacitor type with appropriate ESR ensures the required energy capacity for micro resistance welding, which does not need overly excessive, as in other applications, such as electric vehicles [10] and intermittent wind energy systems [11].

The converter, which controls the charging process of the supercapacitor battery, is designed as a Flyback converter. It partly functions as input current form corrector. It should be noticed that even though the output power of the converter is relatively low (tens of watts), the currents flowing through the considered part of the converter are several amperes and they cause substantial energy losses within individual circuit components. So, this part of the circuit requires an in-depth analysis.

### 3. ANALYSIS OF LOSSES OF THE CHARGING DEVICE

Energy efficiency is one of the key parameters in the design of charging devices. The efficiency of the charging device depends on the operating conditions such as the average value of voltage and current, and the PWM switching frequency. However, the most significant portion of total losses of the charging device is related to dynamic losses in semiconductors and conduction losses that are caused by parasitic resistances. Efficiency is usually expressed as [12]:

$$\eta = \frac{P_{out}}{P_{in}} \cdot 100\% , \quad (4)$$

where  $P_{out} = P_{in} - P_{loss}$  is the device output power of the charging device, and  $P_{in}$  is the input power of the charging device.

As illustrated in Fig. 1, the charging device consists of a bridge rectifier, an input filter, a flyback converter, and a supercapacitor battery. Therefore, according to the proposed method, the total power losses are calculated as the sum of the power losses of each of the aforementioned subsystem of the charging device.

Power losses in the power supply of the charging device (i.e., input rectifier) are mainly caused by the conduction losses within the diodes due to the forward and reverse current flows. Switching (commutation) losses are negligible due to the low frequency of the alternating current supplying the charging device from the utility grid. The voltage drop across the diode and the series resistance are the sources of a diode's conduction losses [12], [13]:

$$P_{VDcond} = I_d^2 \cdot R_{DS} + I_{in} \cdot U_F , \quad (5)$$

where  $I_d$  is the RMS value of the current passing through diode,  $R_{DS}$  is the equivalent resistance of the diode,  $U_F$  is the forward voltage drop and  $I_{out}$  is the input current of the charging device (bridge rectified output current).

During conduction, the power loss in each of the two simultaneously conducting diodes will be the same. Since only a pair of diodes are conducting over one half-period of the grid voltage, the average power loss within the diode bridge rectifier can be calculated as:

$$P_{rectifier} = \frac{2}{T} \int_0^{T/2} 2P_{VDcond} dt = 2P_{VDcond} . \quad (6)$$

Power losses within the input filter generally comprise the inductor and capacitor power losses. Dielectric power losses of the input capacitor  $C_{in}$  can be calculated from the following equation [12]:

$$P_C = U_C \cdot 2\pi fC \cdot \tan \delta , \quad (7)$$

where  $U_C$  is the capacitor voltage,  $C$  is the capacitor capacitance, and  $\tan \delta$  is the dielectric loss angle tangent.

Inductor losses are due to the core hysteresis losses and winding losses, while the eddy current losses are neglected due to the frequency of the voltage at the filter input. In order to calculate the losses in the inductor core, the following equation can be used [14]:

$$P_{Lc} = k \cdot f^\alpha \cdot B^\beta \cdot V_c , \quad (8)$$

where  $f$  is the rectified voltage ripple frequency (twice the grid voltage frequency),  $B$  is the magnitude of flux density variations within the core, and  $k$ ,  $\alpha$  and  $\beta$  are Steinmetz's constants and  $V_c$  is the volume of core material.

The wire (conductor) loss, caused by the Ohmic resistance, is defined by the following formula:

$$P_{Lw} = I_d^2 \cdot R_{DC} , \quad (9)$$

where  $I_d$  is the RMS value of the current passing through inductor, and  $R_{DC}$  is the winding Ohmic resistance.

Power losses of the Flyback converter consist of the transformer losses, MOSFET transistor losses, output Schottky diode losses, and output capacitor losses. Transformer power losses can be categorized as: core hysteresis losses, core eddy current losses, and winding losses.

The hysteresis losses represent the work required in order to alternate the direction of the magnetic flux within the ferromagnetic core. Naturally, these losses strongly depend on the type of material used to build the core. Based on the improved Steinmetz equation, the transformer core power losses  $P_{Trc}$  can also be calculated according to Eq. (6), wherein the parameter  $B$  represents the magnitude of the alternating magnetic field flux density within the core [14]:

$$P_{Trc} = k \cdot f^\alpha \cdot B_m^\beta \cdot V_c . \quad (10)$$

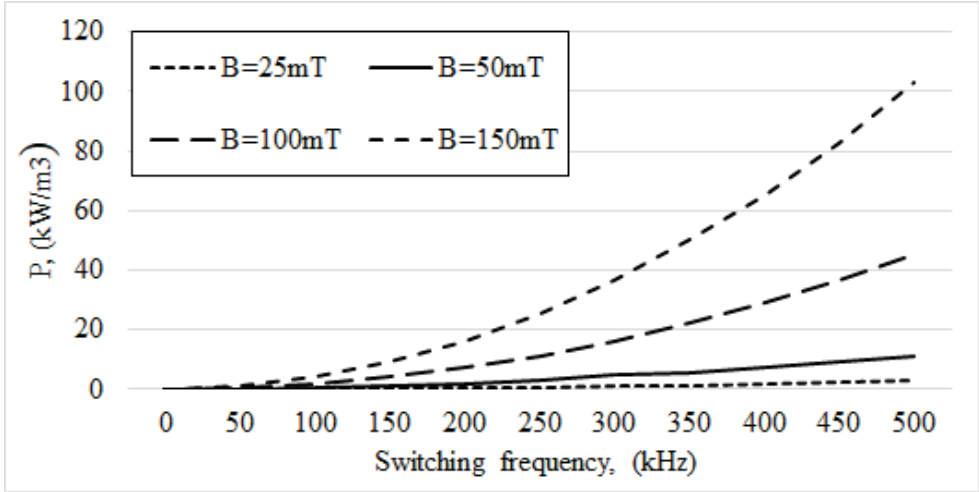


Fig. 3. Core hysteresis frequency power losses for different field flux density magnitudes

The transformer core hysteresis losses are proportional to the Flyback converter switching frequency and to the maximum amplitude (magnitude) of the magnetic field flux density. Figure 3 illustrates the core losses for a selected transformer as a function of field flux density magnitude and frequency. It is apparent that for very low magnitudes of the core field flux density ( $B = 50$  mT), the core losses may be considered negligible up to 100 kHz. However, as the frequency and filed flux density increase, hysteresis losses may have a significant effect on the overall losses of the charging device.

The eddy currents generated by the magnetic field also contribute to the overall losses within the transformer core. The eddy currents flowing within the core will give rise to the so-called magnetic skin effect, which will also be more prominent at higher frequencies. As a consequence, the flux density in the core and the power flow through the transformer are reduced. Figure 4 shows the frequency dependence of the power losses due to eddy currents.

The power losses due to eddy currents are obtained according to the following equation [15]:

$$P_{Tre} = k_e \cdot f^2 \cdot B^2 \cdot V_c, \quad (11)$$

where  $f$  is the power converter PWM switching frequency,  $B$  is the flux density within the core,  $k_e$  is the eddy current coefficient that depends on the type of the core material and  $V_c$  is the volume of the core material.

The magnitude of the winding losses is proportional to the winding resistance, and to the current squared. The magnetic field around the windings will in turn create an electric skin effect, which will increase the effective resistance of the windings, thereby

restricting the current flow to the outer parts of the conductor. The winding power losses can be calculated as [12]:

$$P_{Trw} = \sum_{n=1}^m I_{DCn}^2 \cdot R_{DCn} + \sum_{n=1}^m I_{ACn}^2 \cdot R_{ACn}, \quad (12)$$

where  $I_{DC}$  is the DC current component,  $R_{DC}$  is the winding DC (Ohmic) resistance,  $I_{AC}$  is the AC current component, and  $R_{AC}$  is the winding equivalent AC resistance due to the electric skin effect.

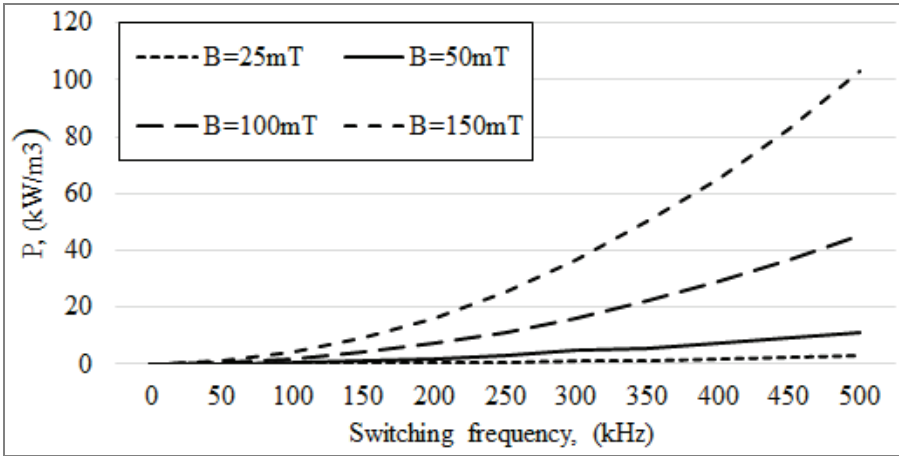


Fig. 4. Eddy current vs. frequency power losses for different magnitudes of field flux density

Conduction losses of the MOSFET transistor are directly dependent on the current passing through the transistor and are very little dependent on the switching frequency. Conduction losses within the power MOSFET can be calculated as [9]:

$$P_{VTcond} = I_d^2 \cdot R_{DS(on)}, \quad (13)$$

where  $I_d$  is the RMS value of the current passing through the transistor, and  $R_{DS(on)}$  is the drain-source on-state resistance.

MOSFET switching losses depend on the load current and the power supply switching frequency according to the following equation [12]:

$$P_{VTsw} = U_{in} \cdot f \cdot (I_D \cdot t_a + 0,5Q_{rr}), \quad (14)$$

where  $U_{in}$  is the drain-to-source voltage,  $I_D$  is the drain current,  $f$  is the switching frequency,  $t_a$  is the reverse recovery time, and  $Q_{rr}$  is the reverse recovery charge.

The conduction losses of the output Schottky diode within the Flyback converter are calculated as follows [11]:

$$P_{VDcond} = I_d^2 \cdot R_{DS} + I_{out} \cdot U_F, \quad (15)$$

where  $I_d$  is the RMS value of the current passing through diode,  $R_{DS}$  is the equivalent resistance at the given junction temperature of the diode,  $U_F$  is the forward voltage drop and  $I_{out}$  is the output current of the Flyback converter.

Finally, dielectric power losses of the output capacitor  $C_{out}$  can be calculated from (7).

The circuit schematic in Fig. 5 represents a simple RC model of a supercapacitor. It comprises three ideal circuit elements: a series resistor  $R_{ESR}$  (i.e. the equivalent series resistor or ESR) which contributes to the energy loss component of the supercapacitor during charging or discharging; a parallel resistor  $R_{leak}$  representing the leakage resistance, and a capacitor  $C_{SC}$  representing the supercapacitor capacitance. The power losses due to the leakage current are significantly lower than the power losses due to equivalent series resistance. Consequently, leakage current losses can be neglected in the analysis [9].

The power losses during charging of the supercapacitor can be calculated as:

$$P_c = i_c^2 \cdot \sum_{k=1}^m R_{ESRk}, \quad (13)$$

where  $i_c$  is the supercapacitor battery charging current and  $R_{ESR}$  is the equivalent series resistor of the  $k$ -th series-connected supercapacitor cell.

Supercapacitor charging current can be expressed by the following equation:

$$i_c = C_{SC} \frac{dU}{dt}, \quad (14)$$

where  $U$  is the voltage across the equivalent capacitor  $C_{SC}$ .

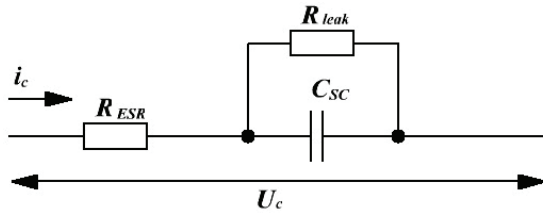


Fig. 5. Equivalent model of a supercapacitor

#### 4. EFFICIENCY OF THE CHARGING DEVICE

Power losses have been evaluated analytically on the basis of the equations discussed in Sections 3. The main components data and parameters of the charging device are reported in Table 2.

Table 2. Data used in power losses analysis

$U_{in}$ , V	$230 \pm 10\%$	$VD1-VD4$	KBP207G	$Tr1$	ferrite core	N87 EFD-25
$U_{out}$ , V	5.5	$C_{in}$	4.7 $\mu$ F, 400 V	$VD5$	STPS40L40CT	
$I_{disch}$ , A	50–500	$L_{in}$	RLB0812-101KL	$C_{out}$	10 $\mu$ F, 100 V	
$f_{sw}$ , kHz	50–500	$VT1$	STB8N65M5	Supercap	Maxwell 350 F 2.5 V	

Based on the equations given in Sections 3, losses as a function of the converter switching frequency are presented in Fig. 6. One of the main sources of conduction losses in the charging device is the output diode VD5. The voltage drops in the open  $p-n$ -junction of the typical diode are 1.2–1.4 V. The problem could be solved application of Schottky diodes, in which the voltage drop is 0.4–0.7 V. Another way to solve the problem could be used a MOSFET transistor as an output diode of a Flyback converter [16].

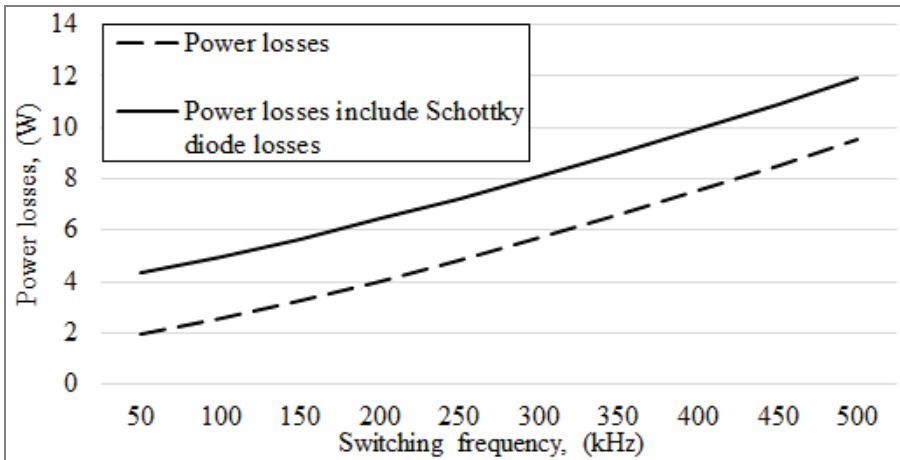


Fig. 6. Power loss as a function of the switching frequency

It should be mentioned that in order to determine the optimal topology of the charging device of Supercap Battery, it is necessary to carry out losses analysis for both topologies with the different values of the switching frequency, since the increase of the switching frequency dramatically increases the dynamic power losses. The function of switching frequency-related power losses in Fig. 7 shows the obtained results of power losses analysis for the Flyback converter topology based on using MOSFET transistor as an output diode.

Figure 8 shows the calculated efficiencies of the charging device for different values of switching frequency. The Flyback converter topology with Schottky diode as output diode achieves an efficiency of 85.0 % at 50 kHz switching frequency for a 28.6 W output power. On the other hand, the proposed converter with MOSFET transistor acting as

the output diode achieves a notably higher efficiency of 92.0 % at the same switching frequency and for equal output power conditions. Therefore, the proposed Flyback converter topology could improve the power efficiency by 7.0 % by minimizing the conduction losses.

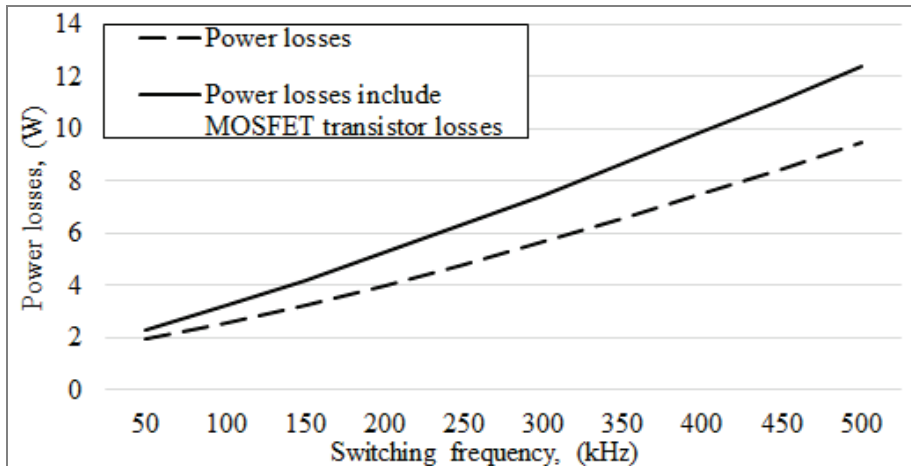


Fig. 7. Power loss as a function of the switching frequency

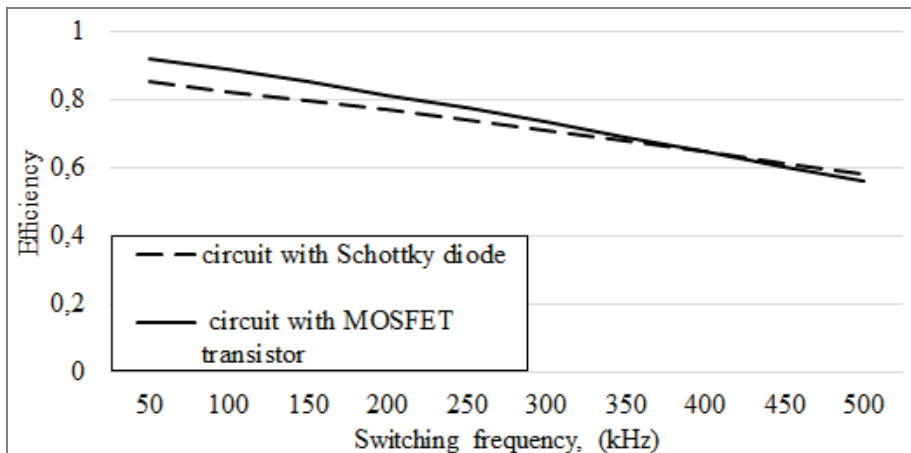


Fig. 8. Comparison of efficiency of the Flyback converter topology with Schottky diode and with MOSFET transistor

It should be noted that the increase in switching frequency increases the dynamic power losses of MOSFET transistor and thereby reduces the gain in efficiency. Fig.8 shows that using the MOSFET transistor as the output diode of the Flyback converter does not seem to be advisable at switching frequencies above 400 kHz.

## 5. CONCLUSIONS

This paper has presented an analysis of power losses within the Flyback converter used as a charging device for the supercapacitor-based energy storage system utilized in micro-resistance welding applications. The analysis results have pointed out to the possibility of notably increasing the efficiency of the charging device. The high-efficiency of the charging device could be provided by reducing the conduction power losses of the Flyback converter. The improved efficiency of the Flyback converter can be achieved by using a MOSFET transistor as an output diode, thus increasing the efficiency by 7.0% at the switching frequency of 50 kHz. However, the application of the MOSFET transistor is inadvisable at switching frequencies above 400 kHz, because the dynamic power losses of the MOSFET transistor increase above those observed for the case of the more traditionally used Schottky diode.

## REFERENCES

- [1] DONG S., KALKA G., ZHOU Y., *Electrode sticking during micro-resistance welding of thin metal sheets*, Electronics Packaging Manufacturing IEEE Transactions, 2002, Vol. 25, No. 4, 355–361, DOI: <http://dx.doi.org/10.1109/ICEPT.2017.8046536>.
- [2] BONDARENKO Yu., SAFRONOV P., BONDARENKO O., SYDORETS V., ROGOZINA T., *The hybrid energy storages based on batteries and ultracapacitors for contact microwelding*, Tekhnologiya i konstruirovaniye v elektronnoi apparature, 2014, No. 4, 33–38 (in Russian), DOI: <http://dx.doi.org/10.15222/TKEA2014.4.33>.
- [3] SHEN J., DUSMEZ S., KHALIGH A., *Optimization of Sizing and Battery Cycle Life in Battery. Ultracapacitor Hybrid Energy Storage Systems for Electric Vehicle Applications*, IEEE Transactions on Industrial Informatics, 2014, Vol. 10, No. 4, pp. 2112–2121, DOI: <http://dx.doi.org/10.1109/TII.2014.2334233>.
- [4] SHIN D., KIM Y., SEO J., *Battery-supercapacitor hybrid system for high-rate pulsed load applications*, Design, Automation & Test in Europe. Grenoble, France. March 2011, 627–632, DOI: <https://doi.org/10.1109/DATE.2011.5763295>.
- [5] CHOI W., YANG M., SUH Y., *High-efficiency supercapacitor charger using an improved two-switch forward converter*, Journal of Power Electronics, 2014, Vol. 14, No. 1, 1–10, DOI: <http://dx.doi.org/10.6113/JPE.2014.14.1.1>.
- [6] YANG M., CHO H., LEE S., CHOI W., *High-efficiency ultracapacitor charger using a soft-switching full-bridge DC-DC converter*, IEEE Applied Power Electronics Conference and Exposition (APEC). Charlotte, USA. March, 2015, 2044–2049, DOI: <http://dx.doi.org/10.1109/APEC.2015.7104630>.
- [7] HRANOV T., VACHEVA G., HINOV N., ARNAUDOV D., *Modeling DC-DC converter for charging supercapacitors*. 40th International Spring Seminar on Electronics Technology (ISSE). Sofia, Bulgaria. May 2017, 1–5, DOI: <http://dx.doi.org/10.1109/ISSE.2017.8001002>.
- [8] KRAEV G., HINOV N., ARNAUDOV D., RANGELOV N., GILEV B., *Serial ZVS DC-DC converter for supercapacitor charging*. 19th International Symposium on Electrical Apparatus and Technologies (SIELA), Bourgas, Bulgaria, May 2016, 193–196, DOI: <http://dx.doi.org/10.1109/SIELA.2016.7543018>.
- [9] YANG H., ZHANG Y., *Analysis of supercapacitor energy loss for power management in environmentally powered wireless sensor nodes*, IEEE Transactions on Power Electronics, 2013, Vol. 28, No. 1, 5391–5403, DOI: <http://dx.doi.org/10.1109/TPEL.2013.2238683>.

- [10] PAVKOVIĆ D., CIPEK M., KLJAIĆ Z., MLINARIĆ T.J., HRGETIĆ M., ZORC D., *Damping Optimum-Based Design of Control Strategy Suitable for Battery*, Ultracapacitor Electric Vehicles, Energies, 2018, Vol.11, No. 10, Paper No. 2854, 26 pp., DOI: <https://doi.org/10.3390/en11102854>.
- [11] PAVKOVIĆ D., CIPEK M., HRGETIĆ, M, SEDIĆ A., *Modeling, parameterization and damping optimum-based control system design for an airborne wind energy ground station power plant*, Energy Conversion and Management, 2018, Vol. 164, pp. 262–276, DOI: <https://doi.org/10.1016/j.enconman.2018.02.090>.
- [12] IVANOVIC Z., BLANUSA B., KNEZIC M., *Power Loss Model for Efficiency Improvement of Boost Converter*. XXIII International Symposium on Information, Communication and Automation Technologies. Sarajevo, Bosnia and Herzegovina, October 2011, 1–6, DOI: <http://dx.doi.org/10.1109/ICAT.2011.6102129>
- [13] CAPITAINE A., PILLONNET G., CHAILLOUX T., KHALED F., ONDEL O., ALLARD B., *Loss analysis of flyback in discontinuous conduction mode for sub-mW harvesting systems*. 14th IEEE International New Circuits and Systems Conference (NEWCAS), Vancouver, Canada, June 2016, 1–4, DOI: <http://dx.doi.org/10.1109/NEWCAS.2016.7604810>.
- [14] SULLIVAN C., HARRIS H., HERBERT E., *Core loss predictions for general PWM waveforms from a simplified set of measured data*. Proc. of Applied Power Electronics Conference and Exposition (APEC), Palm Springs, USA, February 2010, 1048–1055. DOI: <http://dx.doi.org/10.1109/APEC.2010.5433375>.
- [15] FIORILLO F., BEATRICE C., BOTTAUSCIO O., CARMİ E., *Eddy-Current Losses in Mn-Zn Ferrites*, IEEE Transactions on Magnetics, 2014, Vol. 50, No. 1, DOI: <http://dx.doi.org/10.1109/TMAG.2013.2279878>.
- [16] SEMENOV B., *Power Electronics: from simple to complicated*, SOLON-Press, Moscow 2005, 416 (in Russian).



*traveling waves, fault locating,  
cable lines, autoreclosing*

B. KASZTENNY\*, A. GUZMÁN\*,  
M.V. MYNAM\*, T. JOSHI\*

## **CONTROLLING AUTORECLOSING ON OVERHEAD LINES WITH UNDERGROUND CABLE SECTIONS USING TRAVELING-WAVE FAULT LOCATION BASED ON MEASUREMENTS FROM LINE TERMINALS ONLY**

The paper explains principles of fault locating based on traveling waves measured only at line terminals for hybrid lines comprising overhead and cable sections. The paper introduces an adaptive autoreclosing control logic to allow or cancel reclosing based on the location of the fault. The paper includes examples that explain and illustrate these principles.

### **1. INTRODUCTION**

Historically, fault location information has been provided to a line maintenance crew just in time for them to inspect and repair a line after a permanent fault. Today, with impedance-based fault locating widely available in microprocessor-based protective relays integrated with SCADA, system operators have access to fault location information within seconds.

The next step in the practice of fault locating embedded in protective relays is to provide the fault type and accurate fault location information within milliseconds, in order to facilitate control functions such as adaptive control of autoreclosing.

Today, impedance-based fault locators, especially the single-ended ones, do not guarantee enough accuracy under all fault conditions to support controlling the reclosing logic based on the fault location. Also, today's relays do not typically calculate fault location quickly enough to use it for adaptive control of autoreclosing.

---

\* Schweitzer Engineering Laboratories, Inc., 2350 NE Hopkins Court, Pullman, WA 99163 USA,  
e-mail: bogdan\_kasztenny@selinc.com

This paper reviews technical, safety, and economical merits of adaptive autoreclosing based on fault location, and it presents a method for accurate fault locating using traveling waves (TWs) from both terminals of the line to facilitate such location-dependent “surgical autoreclosing” [1]. The paper illustrates the new principles with simulations and test results from a line relay that provides the first-ever adaptive autoreclosing logic controlled by fault location.

## 2. APPLICATIONS AND BENEFITS OF AUTORECLOSING CONTROLLED BY FAULT LOCATION

### 2.1. HYBRID LINES WITH OVERHEAD LINE SECTIONS AND UNDERGROUND CABLE SECTIONS

Hybrid lines comprising overhead line sections and underground cable sections are becoming more common, especially in urban areas. The underground cable sections are typically more expensive and are only used to cross densely populated areas, airports, highways, or terrain where obtaining an above-the-ground right-of-way is difficult for a variety of reasons, including environmental and aesthetic constraints. A hybrid line can have more than one underground cable section.

Many faults on overhead lines are temporary faults, allowing for a high rate of successful autoreclosing [2]. In contrast, all faults on underground cables are permanent faults. Precursors to faults (incipient faults) are transient in nature, but once the solid cable insulation is damaged, it will not restore itself. Autoreclosing for faults on cables is counterproductive; it further damages the cable causing longer and more expensive repair.

Ideally, you would prefer to allow autoreclosing on overhead line sections and to block autoreclosing on underground cable sections of a hybrid line. In single-pole tripping applications, a single-pole trip for a fault on a cable section should be converted into a three-pole trip, and the autoreclosing scheme should not reclose for that fault.

Today, there are no economical solutions to facilitate this application. Reference [3] proposes installing current transformers (CTs) at each transition between a cable and an overhead line section and obtaining current measurement via a fiber-optic connection to one of the line terminals. Using the current measurement at each transition point, the logic implements a differential zone for each cable section and sends a block command to the autoreclosing device if the fault is in one of the cable sections (in one of the differential zones). To avoid electronics and having to bring auxiliary control power to the CTs located along the line, solution [3] uses a piezoelectric element to convert the current signal into a mechanical displacement signal. Further, it uses a Bragg-effect fiber-optic filter to sense the mechanical displacement remotely with the laser source and the associated sensing electronics located at the main line terminal. This solution has the drawback of requiring CTs at each transition point and fiber-

optic cables from each of these CTs to the main line terminal where the autoreclosing device is located.

Another solution to the adaptive control of autoreclosing of hybrid lines is to use fault location information obtained using measurements only at the line terminals. However, impedance-based fault-locating methods do not have adequate accuracy for this application because of a number of factors (see Section 3).

This paper shows that the double-ended TW-based fault-locating method with correction for line nonhomogeneity provides an accurate fault location for adaptive autoreclosing on hybrid lines.

## 2.2. OTHER APPLICATIONS OF ADAPTIVE AUTORECLOSING

### 2.2.1. LINES TERMINATING AT LARGE GENERATING STATIONS

Reclosing for a permanent fault near a generating station has adverse effects on generators and turbines [2]. Large transient torque created when closing on a high-current fault stresses the generator shaft, turbine shaft, their bearings, and other mechanical components of the unit. The best reclosing practice for these lines is to test the line from the remote line terminal (the terminal away from the generating station) and then reclose the circuit breaker at the generator terminal with synchronism-check supervision [2]. Some lines, however, have generating stations close to both terminals. Inhibiting autoreclosing for high-current close-in faults but allowing reclosing for lower-current remote faults reduces the mechanical stress on the generator and the turbine.

### 2.2.2. LINES WITH PUBLIC SAFETY CONCERNS

Reclosing onto a permanent fault creates a second high-energy event at the fault location, in addition to the initial fault. There are several situations when it may be beneficial to avoid reclosing. They include:

- Highly populated areas, such as subtransmission lines sharing the right-of-way with roads or even residential streets. Not reclosing for fault locations where humans are likely to be present improves safety.
- Airports, especially regional airports receiving small airplanes operated by amateur pilots. Not reclosing for fault locations where a small airplane may have inadvertently flown into the line is beneficial.
- Fire-prone terrain such as forests or bush areas, especially in very dry climates or seasons. Not reclosing for faults on these fire-prone stretches of the line reduces the potential of starting large and expensive wildfires.

### 2.2.3. LINES WITH SECTIONS HAVING A LOW SUCCESS RATE OF AUTORECLOSING

Some lines may experience a very low autoreclosing success rate for faults on certain sections depending on construction or surroundings of these sections. Loca-

tion-dependent autoreclosing offers an option to block reclosing for these low-success-rate sections, while allowing reclosing for faults elsewhere on the line.

### 3. FAULT LOCATING ON HYBRID LINES WITH OVERHEAD LINE SECTIONS AND UNDERGROUND CABLE SECTIONS

#### 3.1. LIMITATIONS OF IMPEDANCE-BASED METHODS

Impedance-based fault-locating methods using the total line impedance value of the hybrid line face the following challenges [4]:

- The positive-sequence impedance per mile is very different for the overhead sections and cable sections.
- The  $Z_0/Z_1$  ratio is very different for the overhead sections and cable sections.
- The zero-sequence impedance for cable sections can be a nonlinear function of the fault current, is uncertain, and it depends on the grounding and shielding methods and other conductive paths in the vicinity [4].

In addition, the following common factors affect the accuracy of impedance-based methods in general:

- Ratio errors in CTs and voltage transformers (VTs).
- Phasor measurement errors in the fault-locating device.
- Uncertainty in line impedance data.
- Impact of fault resistance and changes in fault resistance.
- Impact of the line charging current.

As a result of the general accuracy-limiting factors and accuracy-limiting factors specific to cables and hybrid lines, the expected fault-locating accuracy of impedance-based methods in cables or hybrid lines can be on the order of 10 percent or worse, and it is insufficient to support the adaptive autoreclosing application.

#### 3.2. DOUBLE-ENDED TW-BASED FAULT-LOCATING PRINCIPLE

Figure 1 shows a Bewley diagram for a fault at location  $F$  on a line of length  $LL$ . The fault is  $M$  (km or mi) away from the local terminal ( $S$ ) and  $LL - M$  (km or mi) away from the remote terminal ( $R$ ). The TW propagation velocity ( $PV$ ) for the line is the ratio of the total line length ( $LL$ ) and the  $TW$  line propagation time ( $TWLPT$ ) settings of the fault locator:

$$PV = \frac{LL}{TWLPT}. \quad (1)$$

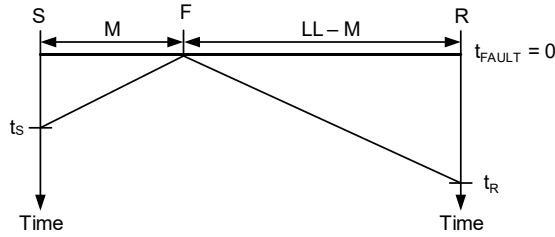


Fig. 1. Bewley diagram explaining double-ended TW-based fault locating.

The first current TW arrives at Terminal S at:

$$t_s = \frac{M}{PV}. \quad (2)$$

The first current TW arrives at Terminal R at:

$$PV = \frac{LL - M}{PV}. \quad (3)$$

Solving (2) and (3) for the fault location,  $M$ , and factoring in (1) for the propagation velocity, we obtain the following fault-locating equation:

$$M = \frac{LL}{2} \left( 1 + \frac{t_s - t_r}{TWLPT} \right). \quad (4)$$

The fault-locating method (4) measures current TWs by using a differentiator-smoother filter [5]. A practical implementation [6] of this method applies the differentiator-smoother filter to current samples taken every microsecond. The method further incorporates a time-stamping algorithm that uses interpolation to find the time of the peak for the output of the differentiator-smoother filter. This interpolation provides a time-stamping accuracy of approximately  $0.1 \mu\text{s}$ , i.e., about ten times better than the sampling interval.

The double-ended TW-based fault-locating method (4) is simple, yet very accurate. It requires identifying and time-stamping only the very first TWs at both line terminals. Not having to isolate and identify the origin of any subsequent TWs is a great advantage of this fault-locating method [5] compared with the single-ended method. Because (4) is a double-ended method, it requires the TW-based fault-locating devices at both line terminals to be synchronized so that the TW arrival times at both line terminals are captured with the same time reference. The synchronization is typically achieved using satellite-synchronized clocks or using a direct point-to-point fiber-optic channel between the devices [1].

The double-ended TW-based fault-locating method (4) has a field-proven track record with reported accuracy within one tower span (300 m or 1000 ft) on average

[5]. When tested under ideal conditions, the double-ended TW-based fault-locating method (4) implemented on a hardware platform [6] yields a 90th percentile error considerably below 20 m (66 ft) and a median error less than 10 m (33 ft).

### 3.3. DOUBLE-ENDED TW-BASED FAULT LOCATING FOR HYBRID LINES

Consider the hybrid line depicted in Fig. 2, comprising two overhead line sections, 1 and 3, and one underground cable section, 2. The overhead section lengths are  $LL_1$  and  $LL_3$  and the cable section length is  $LL_2$ . The TW line propagation times for the overhead line sections are  $TWLPT_1$  and  $TWLPT_3$  and the TW line propagation time for the cable section is  $TWLPT_2$ .

Expect different propagation velocities for the overhead and cable sections as follows:

$$\frac{LL_1}{TWLPT_1} \cong \frac{LL_3}{TWLPT_3} \gg \frac{LL_2}{TWLPT_2} \quad (5)$$

For example, the propagation velocity for the overhead line sections can be approximately 98 percent of the speed of light in free space, while the propagation velocity for the cable section can be as low as 50 percent of the speed of light in free space.

The line of Fig. 2a can be conveniently depicted as a piece-wise linear characteristic representing the relationship between the distance-to-fault and the TW line propagation time to the fault location (Fig. 2b).

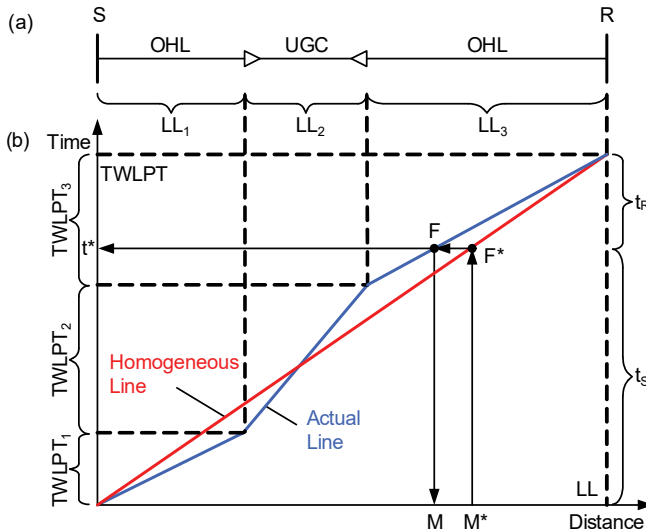


Fig. 2. Sample hybrid line with two overhead sections and one cable section (a) and its distance-propagation time characteristic (b)

Let us denote the total line length as  $LL$ :

$$LL = LL_1 + LL_2 + LL_3 \quad (6)$$

and the total  $TW$  line propagation time as  $TWLPT$ :

$$TWLPT = TWLPT_1 + TWLPT_2 + TWLPT_3. \quad (7)$$

For any fault location ( $F$ ), if one line terminal measures the  $TW$  arrival time as  $t_S$ , the other terminal measures the  $TW$  arrival time as  $t_R = TWLPT - t_S$  (see Fig. 2b).

Assume we use the fault-locating method (4) neglecting the line nonhomogeneity, i.e., we use (4) with the total line length (6) and the total  $TW$  line propagation time (7) as settings and the  $TW$  arrival time difference ( $t_S - t_R$ ) as the measurement. If so, we obtain a fault location ( $M^*$ ) as illustrated in Fig. 2. This fault location is not accurate and represents a fictitious fault ( $F^*$ ) shown in Fig. 2.

Note, however, that the  $TW$  arrival time difference ( $t_S - t_R$ ) applies to the actual fault ( $F$ ) and its true location ( $M$ ). Therefore, we simply correct the result ( $M^*$ ) by projecting it from the straight-line characteristic representing a homogeneous power line in Fig. 2, to the actual line characteristic representing the hybrid line ( $F^* \rightarrow F$  in Fig. 2b).

We summarize our double-ended  $TW$ -based fault-locating method for hybrid (non-homogeneous) lines as follows:

- Step 1. Calculate the fault location ( $M^*$ ) with (4) as if the line were homogeneous, i.e., using the total line length and the total  $TW$  line propagation time.
- Step 2. Calculate the propagation time ( $t^*$ ) corresponding to the fault location ( $M^*$ ) assuming the line is homogeneous, i.e., using the straight line between the origin and the point defined by the total line length and the total  $TW$  line propagation time.
- Step 3. Calculate the actual fault location ( $M$ ) corresponding to the propagation time ( $t^*$ ) using the nonhomogeneity distance-propagation time characteristic of the line.

### 3.4. NUMERICAL EXAMPLE

Consider the hybrid 138 kV line depicted in Fig. 2a with the overhead line sections and underground cable section data given in Table 1.

We modeled this line with an electromagnetic transient program using data for a sample 138 kV overhead line and a 138 kV single-core coaxial underground cable.

Table 1. Hybrid line data used in the numerical example

Section	Type	Length (mi)	Propagation time ( $\mu$ s)
1	Overhead	20.00	107.50
2	Cable	8.00	81.50
3	Overhead	10.00	53.75
Total	Hybrid	38.00	242.75

3.4.1. EXAMPLE 1: FAULT ON THE OVERHEAD SECTION

An AG fault occurred on Section 1 of the overhead line, 15 mi from Terminal *S*. Figure 3 shows the voltages and currents at Terminals *S* and *R*. Figure 4 shows the terminal currents at the time of arrival of the first *TWs*. Figure 5 shows the alpha aerial current referenced to Phase A at the output of the differentiator-smoother filter used to extract the current *TWs* from the measured currents.

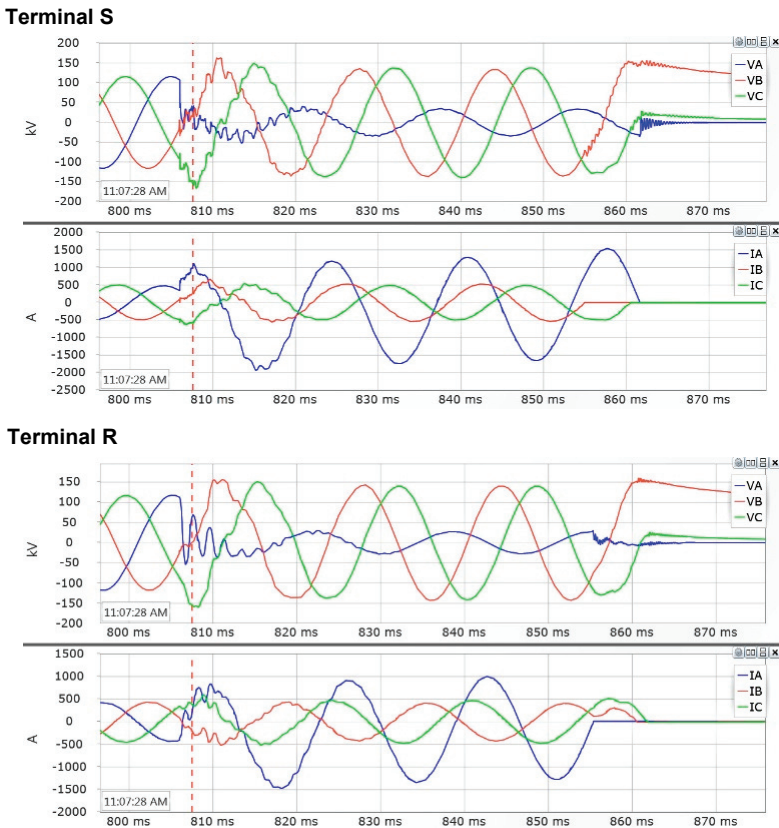


Fig. 3. Example 1: Voltages and currents at Terminals *S* and *R*

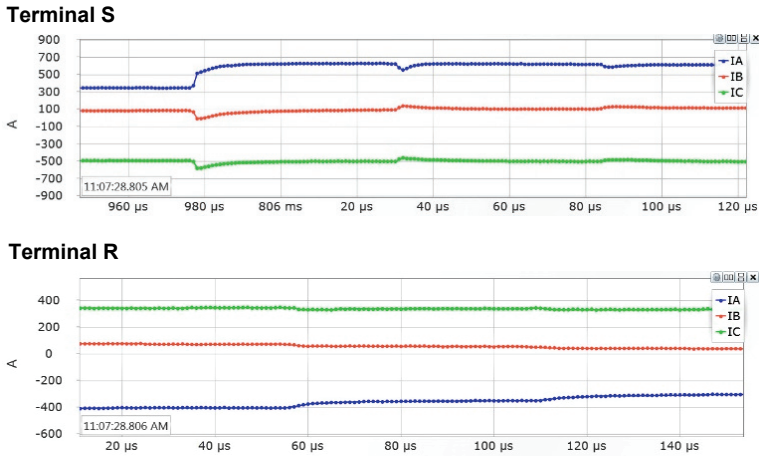


Fig. 4. Example 1: Currents at Terminals *S* and *R* on the time scale selected to show the first *TW*'s arriving at the line terminals

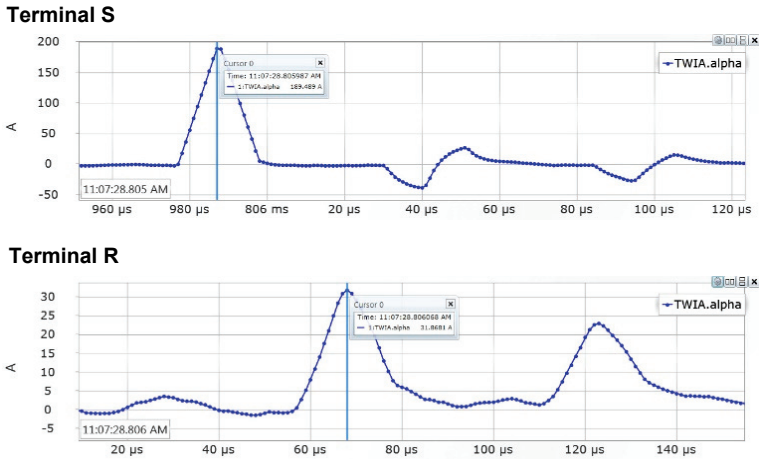


Fig. 5. Example 1: Very first current *TW*'s at Terminals *S* and *R*

The time-stamping algorithm [5] calculates the following *TW* arrival times at Terminals *S* and *R* for the *TW*'s shown in Fig. 5:

$$t_S = 805\,987.549 \mu\text{s} \quad \text{and} \quad t_R = 806\,068.341 \mu\text{s}.$$

Using (4), we calculate the raw fault location as follows (Step 1):

$$M^* = \frac{38}{2} \left( 1 + \frac{5987.549 - 6068.341}{242} 75 \right) = 12.676 \text{ mi.}$$

Assuming a homogeneous line, we obtain the following TW line propagation time from Terminal S to the fault (Step 2):

$$t^* = 12.676 \cdot 242 \frac{75}{38} = 80.976 \mu\text{s}.$$

Using the nonhomogeneity characteristic as per Table 1, we obtain the true fault location (Step 3):

$$80.976 \mu\text{s} \rightarrow 15.066 \text{ mi.}$$

The 0.066 mi error is about 350 ft (107 m), or about one-third of a tower span.

3.4.2. EXAMPLE 2: FAULT ON THE UNDERGROUND SECTION

A BG fault occurred on Section 2 (underground cable), 23 mi from Terminal S or 3 mi from the transition point between Section 1 and Section 2. Figure 6 shows the voltages and currents at Terminals S and R. Figure 7 shows the alpha aerial current referenced to Phase B at the output of the differentiator-smoother filter used to extract the current TWs from the measured currents.

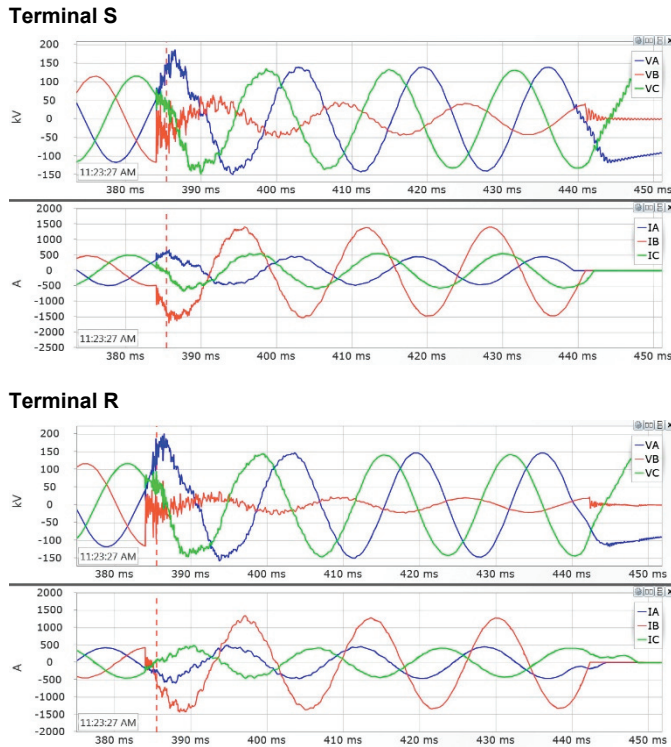


Fig. 6. Example 2: Voltages and currents at Terminals S and R

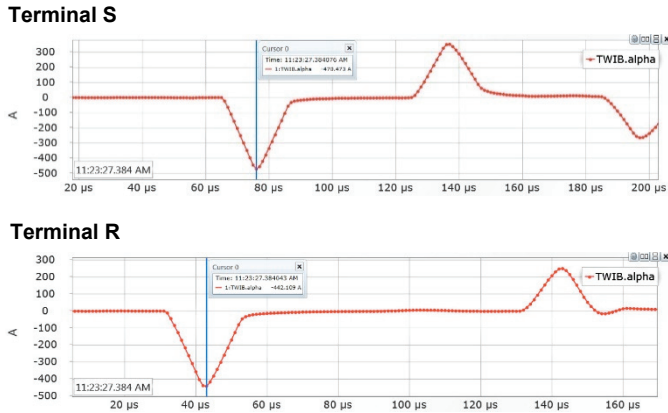


Fig. 7. Example 2: Very first current TWs at Terminals *S* and *R*

The time-stamping algorithm [5] calculates the following *TW* arrival times at Terminals *S* and *R* for the *TW*s shown in Fig. 7:

$$t_S = 384\,076.341\ \mu\text{s} \quad \text{and} \quad t_R = 384\,042.813\ \mu\text{s}.$$

Using (4) and the three-step correction method, we obtain the fault location of 23.008 mi. The 0.008 mi error is about 42 ft (13 m).

#### 4. ADAPTIVE AUTORECLOSING CONTROL LOGIC

In reference to Fig. 8, an adaptive autoreclosing logic provides settings that allow the user to specify multiple blocking regions for autoreclosing. The logic asserts an output bit a few milliseconds after the fault if the calculated fault location falls in any of the blocking regions. Apply this blocking bit as follows:

- Use this bit in your autoreclosing scheme to cancel reclosing.
- In single-pole tripping applications, use this bit to force three-pole tripping for single-line-to-ground (SLG) faults.

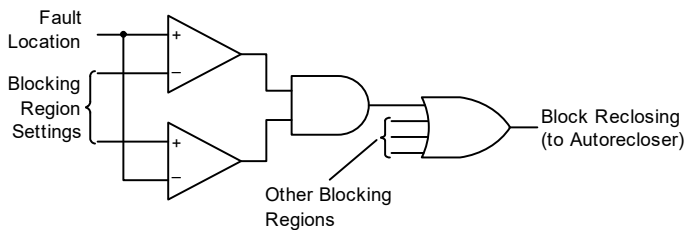


Fig. 8. Simplified autoreclosing control logic

Apply margin when setting the blocking regions to avoid spurious reclosing onto cable faults or onto faults located in the “do not reclose” zones in other applications. Set the blocking region slightly longer than the “do not reclose” stretch of the line. Consult the manufacturer’s fault-locating accuracy specification when selecting margins.

Adaptive autoreclosing control logic may provide a setting to decide if autoreclosing shall be allowed or canceled if the fault-locating algorithm fails to locate the fault for any reason [6].

### 5. OBTAINING CONFIGURATION DATA FOR BETTER ACCURACY OF THE TW FAULT LOCATOR

Line length and TW line propagation time settings impact fault-locating accuracy. This section teaches how to measure the *TW* line (or section) propagation time to improve fault-locating accuracy.

When a power line is being energized, the closure of the circuit breaker pole applies a voltage step to the de-energized conductor, and therefore, it launches a wave that travels to the remote terminal. Because the remote circuit breaker is open, the current TW reflects completely and arrives back at the local terminal.

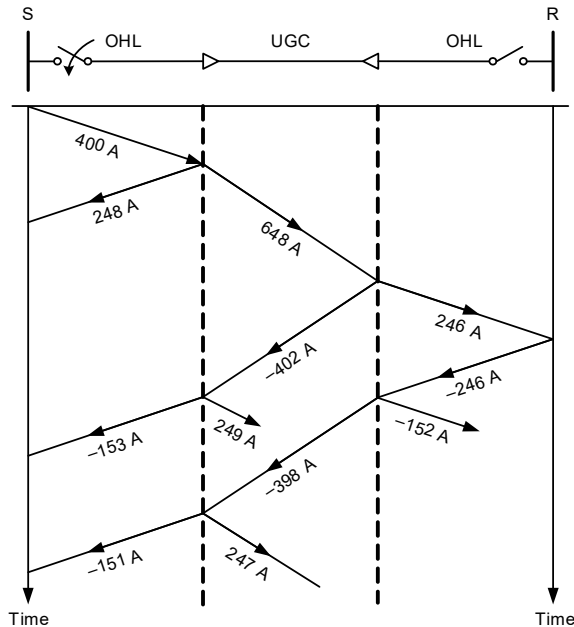


Fig. 9. Incident, reflected, and transmitted TWs for a line energization test of the hybrid line in Table 1

You can use the line energization test to measure the  $TW$  line propagation time for each section of a hybrid line. Each transition between an overhead line section and an underground cable section results in a  $TW$  reflection, i.e., a  $TW$  sent back to the energizing terminal. Figure 9 shows an example of energizing the line of Table 1 assuming 400 A incident current  $TW$ , neglecting dispersion and attenuation, and assuming the overhead line and underground cable characteristic impedances of  $300 \Omega$  and  $70 \Omega$ , respectively. These reflections allow you to measure the  $TW$  line propagation times between the terminal and each significant discontinuity along the line in a manner similar to the time-domain reflectometry method.

Figure 10 shows the  $TW$  signals for line energization from Terminal  $S$  with the incident  $TW$  of about 120 A (compare with Fig. 9 to understand the timing, polarity, and magnitude of the  $TW$ s reflected from the discontinuities of the line). Table 2 shows the  $TW$  arrival time results.

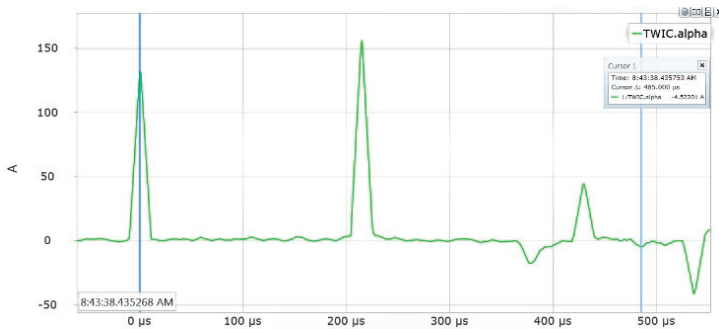


Fig. 10. Example of energizing the line in Table 1 from Terminal  $S$ . Reflections are recorded at 215, 378, and 485  $\mu$ s following the  $TW$  launched by the Phase C pole closure.

The second cursor identifies the reflection arriving at 485  $\mu$ s

Table 2. Propagation times measured during line energization

Section	Round trip	Round trip time ( $\mu$ s)
Energizing from Terminal $S$		
1	From Terminal $S$ to the Section 1–2 transition	215.0
1 + 2	From Terminal $S$ to the Section 2–3 transition	378.0
1 + 2 + 3	From Terminal $S$ to Terminal $R$	485.0

Based on energization from Terminal  $S$ , we obtain these section  $TW$  propagation times:

- Section 1:  $0.5 \cdot 215 \mu\text{s} = 107.5 \mu\text{s}$ ;
- Section 2:  $0.5 \cdot (378 - 215) \mu\text{s} = 81.5 \mu\text{s}$ ;
- Section 3:  $0.5 \cdot (485 - 378) \mu\text{s} = 53.5 \mu\text{s}$ .

Note that the differences between the line energization results and the propagation times in Table 1 are very small, around a quarter of a microsecond.

## 6. CONCLUSIONS

In this paper, we discussed the benefits of using fault location to adaptively control autoreclosing for power lines – to allow reclosing for some fault locations and to prevent reclosing for other fault locations along the line. These applications include blocking autoreclosing for faults on underground cable sections of hybrid lines, line sections in fire-prone rural terrains, near small airports, or in urban areas.

This paper explains how to extend the original double-ended  $TW$ -based fault-locating method derived for homogeneous lines, to hybrid lines in which the cable and overhead sections have different  $TW$  propagation velocities. The method is simple to implement and apply. It requires time synchronization and communications, but only between the main terminals of the line and not between the terminals and each overhead-to-cable transition point. It has accuracy on the order of 300 m (1000 ft) for faults on overhead line sections, and 150 m (500 ft) for faults on cable sections.

The paper presents operation examples from the double-ended  $TW$ -based fault locator integrated with an adaptive autoreclosing control logic implemented in a relay [6].

Performing line energization tests is a recommended practice to obtain accurate settings for the  $TW$ -based fault locator and the adaptive autoreclosing control logic.

## REFERENCES

- [1] KASZTENNY B., GUZMÁN A., MYNAM M.V., JOSHI T., *Locating Faults Before the Breaker Opens – Adaptive Autoreclosing Based on the Location of the Fault*. Proceedings of the 44th Annual Western Protective Relay Conference, Spokane, WA, October 2017.
- [2] C37.104-2002 – IEEE Guide for Automatic Reclosing of Line Circuit Breakers for AC Distribution and Transmission Lines.
- [3] ORR P., FUSIEK G., BOOTH C.D., NIEWCZAS P., DYSKO A., KAWANO F., BEAUMONT P., NISHIDA T., *Flexible Protection Architectures Using Distributed Optical Sensors*. Proceedings of the 11th IET International Conference on Developments in Power System Protection, Birmingham, UK, April 2012.
- [4] TZIOUVARAS D., *Protection of High-Voltage AC Cables*. Proceedings of the 32nd Annual Western Protective Relay Conference, Spokane, WA, October 2005.

- [5] SCHWEITZER E.O., III, GUZMÁN A., MYNAM M.V., SKENDZIC V., KASZTENNY B., MARX S., *Locating Faults by the Traveling Waves They Launch*. Proceedings of the 40th Annual Western Protective Relay Conference, Spokane, WA, October 2013.
- [6] SEL-T400L Time-Domain Line Protection Instruction Manual. Available: <https://selinc.com>

© 2017 by Schweitzer Engineering Laboratories, Inc.  
All rights reserved.  
20171106 • TP6837



*distributed generation, wind generator,  
Heisenberg's uncertainty principle,  
linear approximation,  
Walsh functions, regression analysis*

Kateryna KLEN\*  
Valery ZHUIKOV\*

## **APPROXIMATION AND PREDICTION OF THE WIND SPEED CHANGE FUNCTION**

In the article the features of energy summation from two wind generators, located at a certain distance from each other, are considered. The method of calculating the correlation function between the wind flow speed change functions in the direction of wind distribution is presented. The formulas for describing the fluctuation components of energy at the output of the wind generator are given for two cases: when the phases of the fluctuations of the wind flow on two wind generators are the same and when the fluctuations of the wind flow are in the antiphases. It is shown that to increase the energy level that can be taken from the wind power plant it is necessary to control the phase shift between the energy fluctuations at the output of the wind generators and use the energy of the storages; and to use linear approximations to approximate the wind speed change function. Under the condition of a linear change of the internal resistance of the wind generator in time, it is advisable to introduce the wind speed change function with linear approximations. The system of orthonormal linear functions based on Walsh functions is given. A table with formulas and graphs describing the first 8 functions, which are arranged in order of increasing the number of their sign alternating on the interval of functions definition, is presented. The result of the approximation of the wind speed change function with a system of 8 linear functions based on Walsh functions is shown. Decomposition coefficients, mean-square and average relative approximation errors for such approximation are calculated. In order to find the parameters of multiple linear regression the method of least squares is applied. The regression equation in matrix form is given. An example of application of linear regression prediction method to simple functions is shown. The restoration result for wind speed change function is shown. Decomposition coefficients, mean-square and average relative approximation errors for restoration of wind speed change function with linear regression method are calculated.

---

\* National Technical University of Ukraine "Igor Sikorsky Kyiv Polytechnic Institute", Peremohy Ave. 37, 03056 Kyiv, Ukraine, e-mail: [ekateryna.osypenko@gmail.com](mailto:ekateryna.osypenko@gmail.com)

## 1. INTRODUCTION

The share of electrical energy, generated by renewable energy sources, on the territory of Ukraine is about 2% of the total amount of electrical energy produced [1]. The energy strategy approved by the Government of Ukraine foresees that by 2035 year the share of renewable energy sources in the energy sector will be 11% [2]. The largest share in renewable energy sources in Ukraine is occupied by wind power plants, which in 2016 produced 925 GW\*h of power [3]. A significant increase in the total capacity of wind power plants in Ukraine (more than 100 MW in the last year) requires a case study on increasing of energy efficiency of wind power plants.

The application of Heisenberg's uncertainty principle [4] indicates that in order to maximize the efficiency of wind power plants operation, it is necessary to implement two-channel control: on a basic interval to provide the required level of energy for the charge of the storage (the duration of the basic interval is determined on the basis of specific conditions); on the minimum duration of the observation interval to provide the required level of maximum energy that can be taken from the wind power plants. To implement the selection of maximum energy from a wind power plant it is necessary to take into account the distance between individual wind generators and their mutual influence. The dynamic change in the magnitude and direction of the wind flow speed and, consequently, the internal resistance of the equivalent wind generators source leads to changes in conditions for the maximum energy selection, the basis of which is based on the assumption that the parameters of the source linearly change in time [5]. Effective work of the power plant is realized by predictive control on the basic interval according to the predictor–corrector method [6]. On the  $n$ -th interval there is a prediction of the wind speed change function, and on the  $(n + 1)$ -st interval a correction of values is made, for which one must know the wind speed change function, which requires its approximation with orthogonal functions with the minimum approximation error [7]. In this regard, it is necessary: firstly, to investigate the influence of the distance between the wind generators on conditions for the maximum energy selection; and secondly, to predict wind speed change function considering it's representation by linear approximations.

## 2. CORRELATION BETWEEN WIND SPEED CHANGE FUNCTIONS

Let us consider a simplified scheme of the wind generators  $1 \dots j$  placement (Fig. 1) at a distance from each other, both in the coordinate  $Ox$  and in the coordinate  $Oy$ . In Fig. 1 two possible directions of wind flow are given. In case I, the wind generator 1 is the first on the way to the front of the wind flow, and in the case II, the wind gen-

erator  $j$  is be the first. Each wind generator is connected to the energy summation unit  $\Sigma$  via converter and storage  $C_i$ .

Let us determine the conditions under which, in the case of fluctuations in the wind flow, the selection of maximum energy is ensured. In order to ensure the selection of maximum energy from a wind power plant, it is necessary to consider the mutual influence of the distance between the wind generators on the selection of energy from each of them. For example of two wind generators (1 and 2), with distance  $S$  between them in the direction of propagation of the wind flow. In given case the wind flow is considered uniform with fluctuations relative to some average wind speed. For the consistent work of wind generators a significant correlation function  $C(\tau)$  for the functions of the wind speed  $V_1$  and  $V_2$  is given:

$$C(\tau) = \frac{1}{T} \int_0^T V_1(t)V_2(t + \tau)dt \tag{1}.$$

This function is close to the autocorrelation function with shift  $\tau$ , provided that  $V_1 \approx V_2$ .

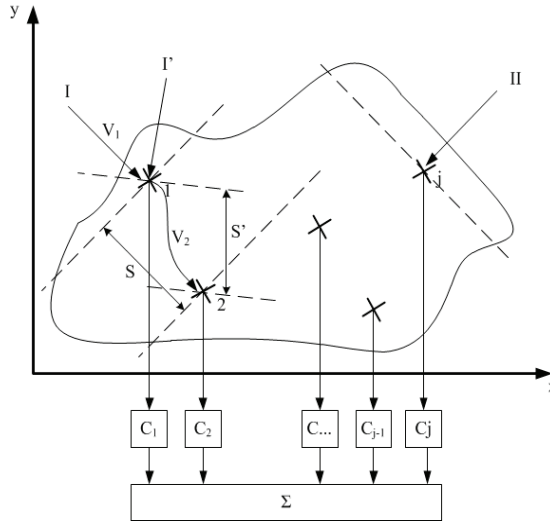


Fig. 1. Simplified scheme of a wind power plant placement

To simplify the calculations, we assume that the wind flow passes distance  $S$  for time  $t_s$  and fluctuations of the wind flow are described by the function  $f_f$  in the sinusoidal law with amplitude  $A_m$  and frequency  $\Omega = 2\pi/T$ ;  $f_f = A_m \sin \Omega t$ . Then the correlation function is determined by the following equation:

$$\begin{aligned}
C(t_s) &= \frac{1}{T} \int_0^T A_m \sin \Omega t \cdot A_m \sin \Omega(t + t_s) dt \\
&= \frac{A_m^2}{4T\Omega} (\sin \Omega t_s - \sin(2\Omega T + \Omega t_s) + 2\Omega T \cos \Omega t_s)
\end{aligned} \tag{2}$$

Correlation function will be equal to 1 if the phases of the fluctuations of the wind flow  $V_1$  and  $V_2$  on the wind generators 1 and 2 are the same. Then the total energy from the two wind generators will be proportional to the wind speed in  $W_w \sim V_3$ , and the total value of the fluctuation energy component at the output of the wind generator  $f_w$  is described as following:

$$f_w = \frac{3}{2} A_m^3 \sin \Omega t - \frac{1}{2} A_m^3 \sin 3\Omega t \tag{3}$$

Since the correlation function depends on the time interval  $\tau$ , then for certain values of this interval, for example, for  $\tau = \pi/2$ , the wind speed change function on the second wind generator will vary according to the cosine law. Then the total value of the fluctuation energy component at the output of the wind generator is described as following:

$$f'_w = \frac{3\sqrt{2}}{4} A_m^3 \sin(\Omega t + 45^\circ) + \frac{\sqrt{2}}{4} A_m^3 \sin(3\Omega t - 45^\circ) \tag{4}$$

Thus, the amplitude of the energy from the fluctuation component decreases in  $\sqrt{2}/2$  times, the pulsation amplitude also decreases, but harmonic pulsations with a frequency of  $3\Omega$  appear. In order to increase the energy that can be taken from a wind power plant, it is necessary to control the phase shift between the energy fluctuations at the output of the wind generators. The energy of the storages can be used to provide the necessary phase and suppress harmonics with a frequency of  $3\Omega$  that can be generated in the supply network.

When changing the direction of the wind (case I'), the distance between the wind generators  $S$  changes accordingly, but the method for estimating the level of energy and pulsations remains the same.

### 3. APPROXIMATION OF WIND SPEED CHANGE FUNCTION

It is known from the approximation theory that with the appropriate choice of approximating functions, the approximation with orthogonal functions provides the least error. Since it is necessary to provide a linear approximation of the wind speed change function, it is expedient to select orthogonal functions that provide such approximation. These functions, in particular, include orthonormal functions of Franklin [8]. But, given their non-periodicity and asymmetry, it is expedient to construct a system of

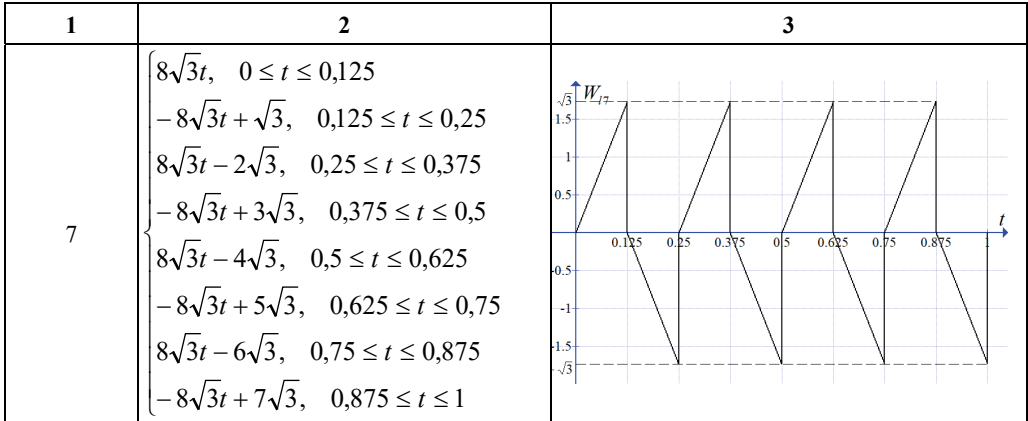
orthonormalized functions  $W_{linear}$  based on Walsh functions, which are constructed in accordance to the following equations:

$$\begin{cases} W_{linear0}(t) = 1 \\ W_{linear i}(t) = (n\sqrt{3} - k\sqrt{3})wal_{nk}(t) \end{cases} \quad (5),$$

where  $i$  – number of piecewise-linear function,  $i = 0, \dots, n$ ;  $n$  – system dimension;  $k$  – number of partitioning interval;  $wal_{nk}(t)$  – value of  $i$ -th Walsh function at the  $k$ -th partitioning interval;  $\{n, k\} = 0 \dots 2^m - 1$ . Given system of functions satisfies the conditions of Gram-Schmidt orthogonalization. These functions, as well as Walsh functions, can be arranged in different ways: by Hadamard, by Rademacher, by Pelley [9]. Table 1 shows the expressions that describe first, fourth and seventh linear functions based on Walsh functions, which are arranged in order of increasing the number of their sign changes in the interval of the functions definition.

Table 1. The system of linear functions based on Walsh functions

Function number, $i$	Formula	Graphical representation
1	2	3
1	$\begin{cases} 8\sqrt{3}t, & 0 \leq t \leq 0,125 \\ 8\sqrt{3}t - \sqrt{3}, & 0,125 \leq t \leq 0,25 \\ 8\sqrt{3}t - 2\sqrt{3}, & 0,25 \leq t \leq 0,375 \\ 8\sqrt{3}t - 3\sqrt{3}, & 0,375 \leq t \leq 0,5 \\ -8\sqrt{3}t + 4\sqrt{3}, & 0,5 \leq t \leq 0,625 \\ -8\sqrt{3}t + 5\sqrt{3}, & 0,625 \leq t \leq 0,75 \\ -8\sqrt{3}t + 6\sqrt{3}, & 0,75 \leq t \leq 0,875 \\ -8\sqrt{3}t + 7\sqrt{3}, & 0,875 \leq t \leq 1 \end{cases}$	
4	$\begin{cases} 8\sqrt{3}t, & 0 \leq t \leq 0,125 \\ -8\sqrt{3}t + \sqrt{3}, & 0,125 \leq t \leq 0,25 \\ -8\sqrt{3}t + 2\sqrt{3}, & 0,25 \leq t \leq 0,375 \\ 8\sqrt{3}t - 3\sqrt{3}, & 0,375 \leq t \leq 0,5 \\ 8\sqrt{3}t - 4\sqrt{3}, & 0,5 \leq t \leq 0,625 \\ -8\sqrt{3}t + 5\sqrt{3}, & 0,625 \leq t \leq 0,75 \\ -8\sqrt{3}t + 6\sqrt{3}, & 0,75 \leq t \leq 0,875 \\ 8\sqrt{3}t - 7\sqrt{3}, & 0,875 \leq t \leq 1 \end{cases}$	



The equation of a function approximated by linear functions based on Walsh functions has the following form [10]:

$$y(t) = \sum_{i=0}^{N-1} c_i W_{linear\ i} \left( \frac{t}{T} \right) \tag{6},$$

where  $c_i = \frac{1}{T} \int_0^1 y(t) W_{linear\ i} \left( \frac{t}{T} \right) dt$  – decomposition coefficients for a series of linear functions based on Walsh functions.

In order to coincide the break points of empirical data and approximating functions, it is expedient to use a system of 8 linear functions based on Walsh functions for approximation.

To predict the wind speed change function, let’s apply the approximation with linear functions based on Walsh functions to the data obtained from [11]. Table 2, as an example, shows the wind speed values for the period from August 31, 2018 to September 7, 2018, which are obtained every 3 hours.

Table 2. Wind speed data, m/s

Time Date	00:00	03:00	06:00	09:00	12:00	15:00	18:00	21:00	00:00
08/31	1	1	2	3	2	2	1	1	1
09/01	1	1	2	3	2	3	2	3	3
...	...	...	...	...	...	...	...	...	...
09/06	1	2	2	3	4	2	2	2	2
09/07	2	2	2	3	1	2	3	1	0

Figure 2 shows the result of the approximation of the wind speed change function on September 7, 2018, with a system of 8 linear functions based on Walsh functions according to equation (6).

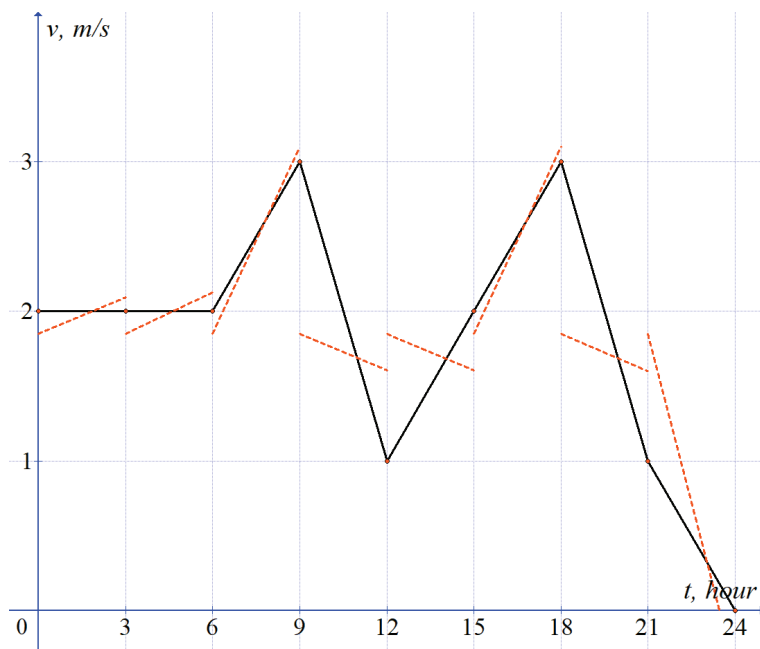


Fig. 2. The result of the approximation of the wind speed change function on September 7, 2018 by a system of 8 linear functions based on Walsh functions

Mean-square approximation error for such decomposition is 79% and average relative approximation error  $\Delta = \frac{1}{N} \sum_i^{N-1} \Delta_i$  in approximation nodes is 30%.

Table 3 shows the values of decomposition coefficients for wind speed change function values given in Table 2.

Table 3. The values of decomposition coefficients for wind speed change function

Coefficient Date	$C_0$	$C_1$	$C_2$	$C_3$	$C_4$	$C_5$	$C_6$	$C_7$
08/31	1.63	0.04	-0.11	-0.04	0.25	-0.11	-0.40	-0.18
09/01	2.25	-0.04	-0.32	-0.04	-0.32	-0.04	-0.18	-0.18
...	...	...	...	...	...	...	...	...
09/06	2.31	-0.07	-0.22	0.14	0.14	-0.22	-0.36	0
09/07	1.88	0.14	0.22	-0.36	0.22	0.07	-0.29	0.14

To predict the wind speed change function, let's predict the decomposition coefficients for a series of linear functions based on Walsh functions. For this regression analysis is applied, and comparison with results of approximation of corresponding empirical data is made.

#### 4. APPLICATION OF REGRESSION ANALYSIS

In order to find the parameters of multiple linear regression let's apply the method of least squares, according to which the decomposition coefficients of a series are calculated by the following equation [12]:

$$B = (C_{in}^T \cdot C_{in})^{-1} C_{in}^T \cdot C_{out}, \quad (7),$$

where  $C_{out}$  – coefficients of a series obtained on  $(n + 1)$ -th observation interval;  $C_{in}$  – coefficients of the series obtained on the  $n$ -th observation interval;  $B$  – coefficients of regression. All coefficients of the equation (4) are presented in the form of the following matrix:

$$C_{out} = \begin{pmatrix} C_1 \\ C_2 \\ \dots \\ C_n \end{pmatrix}, C_{in} = \begin{pmatrix} C_{11}C_{12} \dots C_{1n} \\ C_{21}C_{22} \dots C_{2n} \\ \dots \\ C_{n1}C_{n2} \dots C_{nn} \end{pmatrix}, B = \begin{pmatrix} b_0 \\ b_1 \\ \dots \\ b_n \end{pmatrix}.$$

By solving this system of equations, the matrix-column  $B$  of coefficients of the linear multiple regression is obtained, while the mutual influence of the coefficients was not taken into account.

The system of equations for regression analysis is built as follows. Since the coefficients of the series depend on their values on the previous observation intervals, for each coefficient as input data  $C_{in}$  the coefficients for given number of previous observation intervals and the corresponding coefficient  $C_{out}$  on the current interval were taken. These data form the first equation of the system. Next equations were formed on a similar principle with the displacement of the observation interval to the right. The system of equations is built each time when it is necessary to make a prediction for new empirical data.

With this prediction method for example for 7-th day (September 6, 2018), matrixes  $C_{in}$  and  $C_{out}$  will look as follows:

$$C_{in} = \begin{pmatrix} C_1C_2C_3 \\ C_2C_3C_4 \\ C_3C_4C_5 \end{pmatrix}, C_{out} = \begin{pmatrix} C_4 \\ C_5 \\ C_6 \end{pmatrix}.$$

When obtained the matrix of regression coefficients  $B$  and substituting values ( $C_4C_5C_6$ ) into the regression equation, we obtain values for the 7-th day. For the 9-th day (September 8, 2018) the calculation will be similar. The only difference is that the matrix will have a dimension of  $4 \times 4$ . According to the predicted decomposition coefficients for the 7-th and 9-th days, the decomposition coefficients for the 8-th day (September 7, 2018) is determined as the arithmetic mean of the obtained values (Table 4).

Table 4. Predicted decomposition coefficients for 7-th, 8-th and 9-th days

Coefficient Date	$C_0$	$C_1$	$C_2$	$C_3$	$C_4$	$C_5$	$C_6$	$C_7$
09/06	-0.49	0.13	-0.22	-3.60	0.39	2.23	-0.84	0.01
09/08	2.90	-0.58	27.70	-1.37	0.04	-3.11	3.98	-151.1
<b>09/07</b>	<b>1.21</b>	<b>-0.22</b>	<b>13.74</b>	<b>-2.49</b>	<b>0.21</b>	<b>-0.44</b>	<b>1.57</b>	<b>-75.53</b>

In order to avoid false values in prediction and increase its efficiency, all values out of bounds  $3\sigma$  are considered as false. Instead we use values  $3\sigma$  with a sign corresponding to the sign of the predicted value. Statistical parameters, such as expected value and mean square deviation for 7-th day are given in Table 5.

Table 5. Statistical parameters of decomposition coefficients

Coefficient Parameter	$C_0$	$C_1$	$C_2$	$C_3$	$C_4$	$C_5$	$C_6$	$C_7$
$M$	2.08	-0.01	-0.15	0.06	-0.03	-0.12	-0.29	-0.05
$\sigma$	0.65	0.11	0.24	0.05	0.25	0.17	0.32	0.18
$M - 3\sigma$	0.13	-0.34	-0.87	-0.09	-0.78	-0.63	-1.25	-0.59
$M + 3\sigma$	4.03	0.32	0.57	0.21	0.72	0.39	0.67	0.49

Given this predicted decomposition coefficients for the 7-th, 8-th and 9-th days are shown in Table 6.

Table 6. Corrected predicted decomposition coefficients for 7-th, 8-th and 9-th days

Coefficient Date	$C_0$	$C_1$	$C_2$	$C_3$	$C_4$	$C_5$	$C_6$	$C_7$
09/06	0.13	0.13	-0.22	-0.09	0.39	0.39	-0.84	0.01
09/08	2.90	-0.34	0.57	-0.09	0.04	-0.63	0.67	-0.59
<b>09/07</b>	<b>1.52</b>	<b>-0.11</b>	<b>0.17</b>	<b>-0.09</b>	<b>0.21</b>	<b>-0.12</b>	<b>-0.09</b>	<b>-0.29</b>

The regression equations for the corresponding decomposition coefficients are summarized in Table 7.  $C_i$  is the predictive value of the coefficient, and  $C_{i-1} \div C_{i-4}$  are the values on the previous observation intervals.

Table 7. Regression equations for the corresponding decomposition coefficients

Coefficient	Equation
$C_0$	$C_{0i} = 1.15 \cdot C_{0(i-4)} - 0.09 \cdot C_{0(i-3)} + 0.02 \cdot C_{0(i-2)} - 0.05 \cdot C_{0(i-1)}$
$C_1$	$C_{1i} = 2.11 \cdot C_{1(i-4)} - 0.42 \cdot C_{1(i-3)} - 1.14 \cdot C_{1(i-2)} - 1.2 \cdot C_{1(i-1)}$
$C_2$	$C_{2i} = -33.4 \cdot C_{2(i-4)} - 0.9 \cdot C_{2(i-3)} + 12.23 \cdot C_{2(i-2)} + 31.68 \cdot C_{2(i-1)}$
$C_3$	$C_{3i} = -7.42 \cdot C_{3(i-4)} + 0.37 \cdot C_{3(i-3)} + -0.75 \cdot C_{3(i-2)} + 0.61 \cdot C_{3(i-1)}$
$C_4$	$C_{4i} = -0.23 \cdot C_{4(i-4)} - 0.23 \cdot C_{4(i-3)} - 0.49 \cdot C_{4(i-2)} + 0.25 \cdot C_{4(i-1)}$
$C_5$	$C_{5i} = 4.79 \cdot C_{5(i-4)} - 4.83 \cdot C_{5(i-3)} + 2.17 \cdot C_{5(i-2)} - 0.28 \cdot C_{5(i-1)}$
$C_6$	$C_{6i} = -1.54 \cdot C_{6(i-4)} + 1.21 \cdot C_{6(i-3)} + 2.02 \cdot C_{6(i-2)} + 1.77 \cdot C_{6(i-1)}$
$C_7$	$C_{7i} = 298.85 \cdot C_{7(i-4)} - 97.25 \cdot C_{7(i-3)} - 261.04 \cdot C_{7(i-2)} - 153.6 \cdot C_{7(i-1)}$

According to predicted values of decomposition coefficients, let's restore the wind speed change function for the 8-th day (September 7, 2018). The restoration result is shown in Fig. 3, where the dashed line denotes a function restored by the predicted coefficients, solid line denotes empirical data.

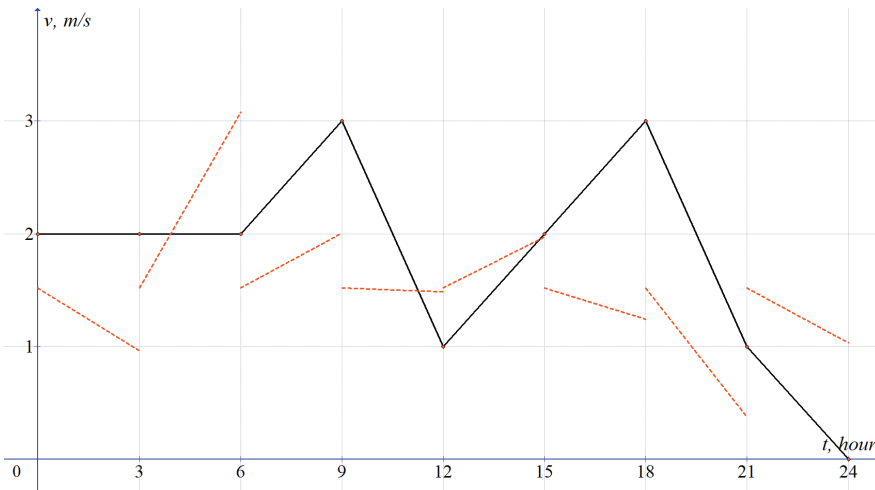


Fig. 3. The restoration result for wind speed change function for the 8-th day (September 7, 2018)

In general, the approximate function can be used to observe the main trend (character of change) of the function on each approximation interval.

Mean-square approximation error for such restoration is 88% and average relative approximation error in approximation nodes is 40%.

The graph shows that at the ends of the interval, the deviations of approximating values are maximum. This is similar to the Gibbs phenomenon [13]. Taking it into account, the mean square approximation error decreases to 33%, and the average relative approximation error in approximation nodes decreases to 23%. Approximation error can be reduced by correction the predicted decomposition coefficients according to a form of wind speed change function.

## 5. CONCLUSIONS

Thus, in order to increase the energy that can be taken from wind generators, it is necessary to fulfill several conditions. First, to control the phase shift between the functions of the energy fluctuations at their outputs. Second, to use the energy of converters and storages to suppress harmonics with a frequency of  $3\Omega$  that can be generated in the supply network. Third, to use linear approximations, for example, the linear functions based on Walsh functions, to approximate the wind speed change function. The application of regression analysis methods to the decomposition coefficients of a series of linear functions based on Walsh functions allows with error of not more than 33% to predict the wind speed change function with the possibility to reduce the value of error by correction the predicted coefficients according to a form of wind speed change function.

## REFERENCES

- [1] SUHODOLYA L., *Current state, problems and prospects of hydropower development in Ukraine*, National Institute for Strategic Studies, Analytical report, 2014.
- [2] Ostap Semerak: *Ukraine pledged to increase its share of renewable energy up to 11% by 2035* [electronic resource] – Access to the resource: <https://www.kmu.gov.ua/ua/news/ostap-semerak-ukrayina-zobovyazalasya-do-11-zbilshiti-chastku-vidnovlyuvanoyi-energetiki-do-2035-roku>
- [3] PRAHOVNYK A., *Harmony of Ukraine's energy and energy efficiency paths to world trends*, Knowledge, Kyiv 2003, p. 100.
- [4] OSYPENKO K., ZHUIKOV V., *Heisenberg's uncertainty principle in evaluating the renewable sources power level*, Technical Electrodynamics, 2017, Vol. 1, pp. 10–16.
- [5] ZHUIKOV V., OSYPENKO K., *Compensator currents form determination considering wind generator aerodynamic resistance*, 2014 IEEE International Conference on Intelligent Energy and Power Systems (IEPS), 2014, pp. 168–170.
- [6] BUTCHER J. C., *Numerical Methods for Ordinary Differential Equations*, John Wiley & Sons, New York 2003.
- [7] KORN G., KORN T., *Mathematical handbook for scientists and engineers*, Science, Moscow, USSR, 1974.
- [8] OSYPENKO K., ZHUIKOV V., *The linearization of primary energy flow parameters change function Franklin discrete functions*, Electronics and Communication, 2016, Vol. 4, pp. 33–37.

- [9] TRAHMAN A., TRAHMAN V., *The fundamentals of the theory of discrete signals on finite intervals*, Soviet radio, Moscow, USSR, 1975.
- [10] DAGMAN E., *Fast discrete orthogonal transformations*, Science, Novosibirsk 1983.
- [11] *The weather at the airports* [electronic resource] – Access to the resource: <http://pogoda.by/avia/?icao=UKBB>
- [12] *Multiple linear regression. Improving the regression model* [electronic resource] – Access to the resource: [https://function-x.ru/statistics\\_regression2.html](https://function-x.ru/statistics_regression2.html)
- [13] BRILLOUIN L., *Science and the information theory*, State publishing house of physical and mathematical literature, Moscow, USSR, 1960.

Janusz SZAFRAN\*  
Eugeniusz ROSOŁOWSKI\*\*

## **DYNAMICALLY CORRECTED FAST ESTIMATORS OF ACTIVE AND REACTIVE POWER AND THEIR PERFORMANCE**

Development of several fast estimators of active and reactive power is presented. The estimators are considered from the point of view of the fast measurement of criteria values in power system automation devices. The main idea of the method is dynamical correction of transients realized thanks to recognition of fault instant and taking into consideration of post fault samples only. In the case of reactive power it is possible to get unique transient response and to realize dynamical correction. Increasing filter window starting from fault instant allows to get better accuracy of estimation in presence of noise. Having small noise it is possible to estimate the reactive power starting from one sample and the active power from two samples of increasing data window. The functions of dynamical correction can be calculated analytically or by using a digital simulation

### 1. INTRODUCTION

Protection and control of power system and its elements requires information concerning many electrical quantities. Changes in the system structure, increasing number and types of sources, many nonlinear elements cause distortion of voltages and currents extremely high in case of faults i.e. during operation of protection systems. Development of digital protection system must follow the changes causing fast and reliable recognition of abnormal states of system elements and the system itself. Digital power system protection is a complex measurement and decision making device. To make decision concerning protected element measured criterion values are used. Both digital processes must be fast, safe and reliable.

---

\* Faculty of Technology and Computer Science, Wrocław University of Science and Technology, Wrocław, Poland, e-mail: janusz.szafran@pwr.edu.pl

\*\* Department of Electrical Power Engineering, Wrocław University of Science and Technology, Wrocław, Poland, e-mail: eugeniusz.rosolowski@pwr.edu.pl

Synthesis of measurement algorithms is made assuming signal containing fundamental component of current and voltage as well as noise. The most popular algorithms are based on estimation of orthogonal components of the signals [4], [5] and Fourier technique. These can be realized using FIR filters which are especially simple in design and application.

The problem of FIR filters is such that they introduce a delay equal the data window. The longer the window the higher the delay and possible solution is either short or variable data window [3], [6], [8]. Short data window gives impaired frequency response producing sometimes high errors of estimation due to noise. Variable data window gives in general high computational burden.

The solution presented in the paper uses variable data window, however, with small computational burden thank to dynamical correction. As usual we must recognize fault instant but later we realize transient which is unique and fault independent. Estimator works very fast in few samples increasing accuracy with time until steady state is reached in time equal to filter window. During transients one coefficient only must be used to realize mentioned dynamical correction.

## 2. FUNDAMENTALS OF POWER ESTIMATORS

Let us assume that voltages and currents can be presented in the form of complex model 0 0:

$$\underline{x}(k) = x_c(k) + jx_s(k) = X \exp(j(k\vartheta + \beta)) \quad (1)$$

where:  $\vartheta = \omega_1 T_s = \frac{2\pi}{N_1}$ ,  $\omega_1$  – frequency of fundamental component,  $T_s$  – sampling period,  $N_1$  – number of samples in one period of fundamental component:  $T_1 = 2\pi/\omega_1$ .

Assuming that imaginary part of the signal (1) is observed, voltages and currents are given by the equations

$$\begin{aligned} v(k) &= V \sin(\vartheta k + \beta) \\ i(k) &= I \sin(\vartheta k + \beta - \varphi) \end{aligned} \quad (2)$$

Fundamental electrical quantities especially active and reactive power, voltage and current magnitudes as well as impedance components and frequency can be measured using orthogonal components voltages and currents (real and imaginary part of the signal (0)). The components can be calculated processing signals by Fourier digital FIR filters.

The model (1) is useful to analysis and synthesis of mentioned above estimators of fundamental electrical quantities being also protection criterion values.

Estimators of power can be found analyzing following equations:

$$(P(k) + jQ(k))\exp(j\vartheta m) = \frac{1}{2}(\underline{v}(k)\underline{i}^*(k-m)) \quad (3)$$

$$(P(k) + jQ(k))\exp(-j\vartheta m) = \frac{1}{2}(\underline{v}(k-m)\underline{i}^*(k)) \quad (4)$$

where:  $m$  – number of delay samples,  $*$  – denotes conjugate value.

Voltage and current in (3), (4) have the form of (1) and their components may be easily estimated by application of non-recursive filters:

$$\begin{aligned} v_c(p) &= \sum_{i=0}^{M-1} h_c(i)v(p-i), \\ v_s(p) &= \sum_{i=0}^{M-1} h_s(i)v(p-i), \end{aligned} \quad \text{where } M = \begin{cases} p & \text{for } p < N_1 \\ N_1 & \text{for } p \geq N_1 \end{cases} \quad (5)$$

for voltage and similarly for current. Impulse functions in (5) can be selected to modify the filters characteristics. In so called Fourier algorithm [6] these functions have the cosine, sine form, e.g.:

$$h_c(i) = \frac{2}{N_1} \cos((i+1-N_1)\vartheta), \quad h_s(i) = \frac{2}{N_1} \sin((i+1-N_1)\vartheta) \quad (6)$$

The constant  $2/N_1$  is the scaling coefficient to determine the proper values for estimated signals (5) in steady-state (for full-period window width).

Substituting voltages and currents in the form (1), adding sides of the equations and rearranging one can get four following equations describing estimators of active and reactive power:

$$P = \frac{1}{2\cos(m\vartheta)}(v_s(k)i_s(k-m) + v_c(k-m)i_c(k)) \quad (7)$$

$$Q = \frac{1}{2\cos(m\vartheta)}(v_s(k)i_c(k-m) - v_c(k-m)i_s(k)) \quad (8)$$

$$P = \frac{1}{2\sin(m\vartheta)}(v_s(k)i_c(k-m) - v_s(k-m)i_c(k)) \quad (9)$$

$$Q = \frac{1}{2\sin(m\vartheta)}(v_f(k-m)i_f(k) - v_f(k)i_f(k-m)) \quad (10)$$

The equations above represent algorithms of power measurement assuming identical window, usually full cycle of fundamental component, of orthogonal sine, cosine filters. In the last equation such orthogonal filters are not necessary, instead we can use any identical filters including IIR. Introducing delay allows to get some variants of the algorithms. Sometimes it must differ from zero.

The algorithms, in general give the accurate value when all samples of measured signals appear inside filters window, simple it give accurate steady state value. On the other hand when these measured values are applied to control and protection systems they work during dynamical conditions. Simply because of either control action or because of faults currents and voltages change rapidly. In such cases signals include samples of voltages and currents before and after fault. Measure values are wrong until inside the window appear all samples after the fault. The solution can be shorter data window, however, it is necessary to recognize fault instant. But remain the problems of greater errors due to noises for shorter windows and orthogonality for any data window length.

These disadvantages and algorithms complexity can be avoided using dynamical correction. To realize the idea two things are necessary: to recognize fault instant, as mentioned before and to develop algorithms having measured values independent on initial phase shift of voltages and currents. The first thing allows to put into the window the signal after the fault only assuming zero signals before, i.e., simply giving always the same zero initial conditions.

On the other hand introductory calculations and tests of algorithms (7)–(10) proved that phase independent transients have both algorithms of reactive power. Both of them will be analyzed and tested below.

### 3. FAST DYNAMICALLY CORRECTED POWER ESTIMATORS

#### 3.1. REACTIVE POWER ESTIMATORS

As it was written the two reactive power estimators are initial phase independent assuming zero initial conditions. Simpler, in general seems to be the forth one from (7)–(10). This requires two identical filters, one to current and the second to voltage and two simple samples delay. The filters can be arbitrary chosen: sin, cos, low pass, no filter as well as any arbitrary IIR filter. On the other hand the second algorithm requires four orthogonal filters so has greater computational burden but signal delay can be avoided so could be one sample faster.

$$Q = \frac{1}{2\sin(m\vartheta)} \left( v_f(k-m)i_f(k) - v_f(k)i_f(k-m) \right) \quad (11)$$

The estimators operate in dynamical conditions when measured criterion values of signals parameters change rapidly. To find dynamical features of the estimator let us assume that at the instant  $p$  equal to zero the input signals of the filter F are voltage and current given by (0). Signals  $v(p)$  and  $i(p)$  can then be described as follows:

$$v(p) = 1(p)v(p); i(p) = 1(p)i(p) \quad (12)$$

$$\text{where: } 1(p) = \begin{cases} 1 & \text{for } p \geq 0 \\ 0 & \text{for } p < 0 \end{cases}.$$

If the filters had zero initial conditions then their output signals are given by the equations:

$$\begin{aligned} v_f(p) &= V(a(p)\sin(\vartheta p + \beta) - b(p)\cos(\vartheta p + \beta)) \\ i_f(p) &= I(a(p)\sin(\vartheta p + \beta - \varphi) - b(p)\cos(\vartheta p + \beta - \varphi)) \end{aligned} \quad (13)$$

$$\text{where: } a(p) = \sum_{i=0}^{p-1} h(i)\cos(\vartheta i), \quad b(p) = \sum_{i=0}^{p-1} h(i)\sin(\vartheta i), \quad h(i) - \text{filter impulse function.}$$

Substituting (13) to (11) one can get:

$$Q = Q(p)T(p) \quad (14)$$

$$\text{where } Q = \frac{1}{2}VI\sin(\varphi).$$

$$\begin{aligned} T(p) &= a(p)a(p-m) + b(p)b(p-m) \\ &+ (a(p)b(p-m) - a(p-m)b(p))\cos(m\vartheta) / \sin(m\vartheta) \end{aligned} \quad (15)$$

Function  $T(p)$  does not depend on initial phase shift of the signals. Functions  $a(p)$ ,  $b(p)$  can be determined analytically for a given filter impulse function. Assuming  $h(i) = h_c(i)$  (6) one obtains from (13):

$$\begin{aligned} a(p) &= \frac{\sin(2p\vartheta) + p\sin 2\vartheta}{2N_1\sin\vartheta} \\ b(p) &= \frac{\sin^2(p\vartheta) - p\sin^2\vartheta}{N_1\sin\vartheta} \end{aligned} \quad (16)$$

Substitution (16) into (15) after some simplification yields the following relation:

$$T(p) = \frac{1}{N_1^2} \left( k(j-m) + \frac{1}{\sin \vartheta \sin(m\vartheta)} \left( k \sin((j-m)\vartheta) \sin((j+1)\vartheta) - (j-m) \sin(k\vartheta) \sin((k-m+1)\vartheta) \right) \right), \quad (17)$$

where:

$$k = \begin{cases} p & \text{for } p < N, \\ N & \text{otherwise,} \end{cases} \quad j = \begin{cases} p & \text{for } p < (N+m), \\ N & \text{otherwise,} \end{cases} \quad T(p) = 0 \quad \text{for } p \leq m,$$

Since the function is unique it is possible to make dynamical correction of the estimator (11).

Combining equations (11) and (14) one can get dynamically corrected estimator of reactive power:

$$Q(p) = \frac{1}{2T(p)} \left( v_f(p-m) i_f(p) - v_f(p) i_f(p-m) \right) \quad (18)$$

The function  $T(p)$  depends on the filters used only and for any arbitrary filter can be either calculated according to (17) (or similar relation obtained for other applied filter) or found by numerical simulation. The structure of reactive power estimator is shown in Fig. 1 and responses of reactive power estimators for full-cycle non-recursive cosine filters: uncorrected and corrected according to (18) (with applied delay  $m = 5$  and  $N_1 = 64$  samples/period) are shown in Fig. 2. It can be seen that in fact (17) represents two-parts function with division point for  $p = N_1$ .

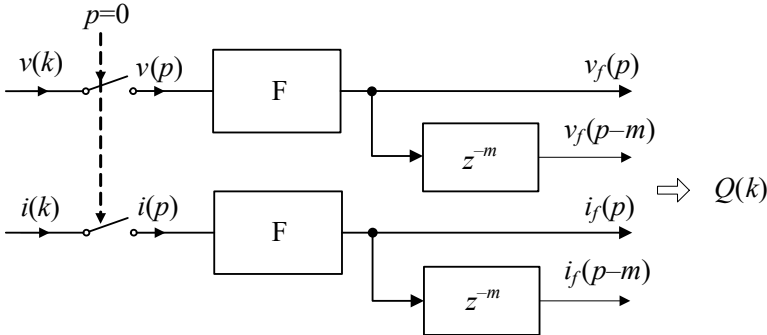


Fig. 1. A structure of reactive power estimator

Similar to described above dynamically corrected reactive power estimator can be obtained using sine, cosine orthogonal components and (8). Assuming for instance delay  $m$  equal to zero one can get:

$$Q = \frac{1}{2}(v_s(k)i_c(k) - v_c(k)i_s(k)) \quad (19)$$

In this case instead of any filter we use a pair of orthogonal filters, however, a delay can be avoided.

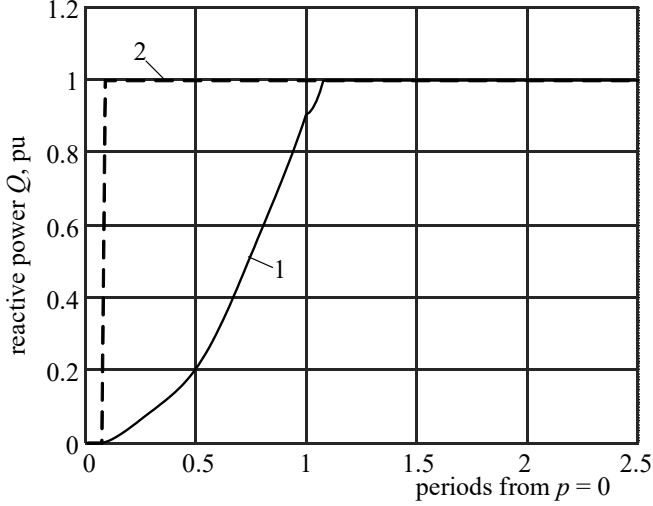


Fig. 2. Time responses of reactive power estimator: 1) typical uncorrected, 2) dynamically corrected; delay  $m = 5$ ,  $N_1 = 64$  samples/period

The structure of this reactive power estimator is shown in Fig. 3. It is seen that we must use zero initial condition of a pair of orthogonal filters identical for voltage and current and having the same increasing window. The procedure starts when fault has been recognized – see (12). Now the signals can be written similarly to (13) in the form:

$$\begin{aligned} v_c(p) &= V(a_c(p)\sin(\vartheta p + \beta) - b_c(p)\cos(\vartheta p + \beta)) \\ v_s(p) &= V(a_s(p)\sin(\vartheta p + \beta) - b_s(p)\cos(\vartheta p + \beta)) \\ i_c(p) &= I(a_c(p)\sin(\vartheta p + \beta - \varphi) - b_c(p)\cos(\vartheta p + \beta - \varphi)) \\ i_s(p) &= I(a_s(p)\sin(\vartheta p + \beta - \varphi) - b_s(p)\cos(\vartheta p + \beta - \varphi)) \end{aligned} \quad (20)$$

where:  $a_n(p) = \sum_{i=0}^{p-1} h_n(i)\cos(\vartheta i)$ ,  $b_n(p) = \sum_{i=0}^{p-1} h_n(i)\sin(\vartheta i)$ ,  $n$  – means  $c$  or  $s$ , adequately, and  $h_c(i) = A\cos(\vartheta i)$ ,  $h_s(i) = A\sin(\vartheta i)$ ,  $A = 2 / N_1$ .

Substituting (20) to (18) one can obtain:

$$Q = Q(p)T(p) \tag{21}$$

where:  $Q = \frac{1}{2}VI \sin(\varphi)$ ,  $T(p) = a_c(p)b_s(p) - a_s(p)b_c(p)$ .

Function  $T(p)$  does depend on initial phase shift of signals just allowing for dynamical correction as before:

$$Q(p) = \frac{Q}{T(p)} = \frac{v_s(p)i_c(p) - v_c(p)i_s(p)}{2T(p)} \tag{22}$$

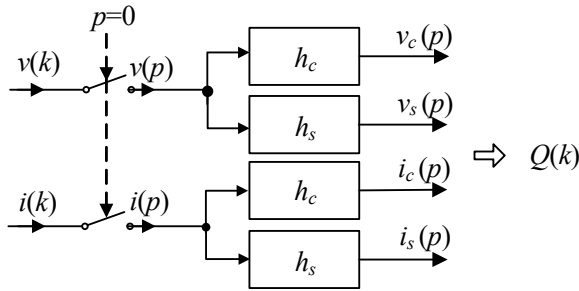


Fig. 3. A structure of second type of reactive power estimator

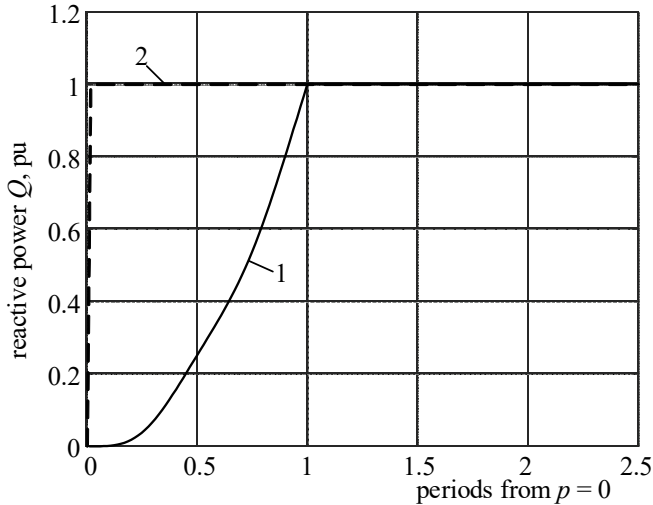


Fig.4. Time response of second type of reactive power estimator:  
 1) uncorrected, 2) dynamically corrected;  
 standard full cycle Fourier (cosine/sine) filters in both cases,  $N_1 = 64$

The function  $T(p)$  depends on the orthogonal filters used and for any filters used can either be calculated or found by numerical simulation. Responses of estimators with dynamical correction and without it applying non-recursive full cycle sine-cosine filters are shown in Fig. 4.

### 3.2. ACTIVE POWER ESTIMATORS

Such simple results cannot be obtained for remaining estimators of protection criterion values. Time response always depend on initial phase shifts and the response is not unique and it is impossible to find a function similar to  $T(p)$ .

However, the worked out estimators can be used to estimate the active power very simple. To do that one of the signals of reactive estimator (voltage or current) must be changed. It is enough for instance to introduce the phase shift of  $\pi/2$  to current. Such shifting means of course the delay of certain number of samples and estimation time increases, however, that time can be limited to single sample. The phase changing on  $\pi/2$  can be obtained if, for instance, the signal is processed according to the equation [2], [7]:

$$i_d(k) = \frac{i(k-n) - i(k)\cos(\vartheta n)}{\sin(\vartheta n)} \quad (23)$$

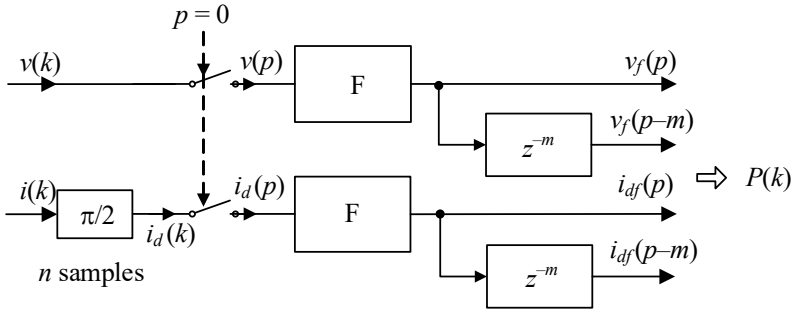


Fig. 5. A structure of active power estimator

A structure of active power estimator is presented in Fig. 5 where  $Q$  estimator would be anyone of two described before. Time response of active power estimators using dynamical correction with delay  $m = 5$  samples and  $n = 10$  samples for introducing the phase shifting according to (23) is presented in Fig. 6b). The applied correction function is the same as in (17). Selection of the introduced delay samples:  $m$  and  $n$  will influence on the frequency response of the final algorithm, however, it is seen that it is possible to get one sample of additional delay only. For comparison with the standard algorithm (7) Fig 6a) presents result of active power estimation without correction during transient period. Shaded area shows changing of the response for different initial phase.

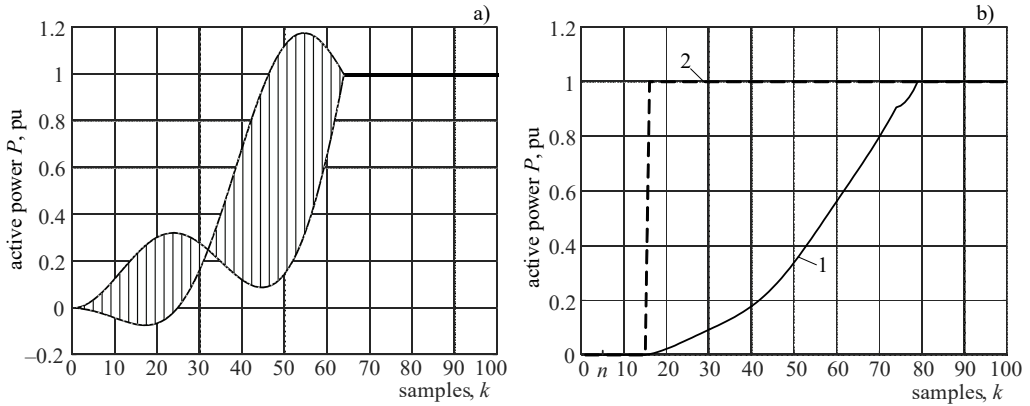


Fig. 6. Time responses of active power estimators: a) applied the first algorithm of active power estimation, b) applied the second algorithm; 1 – typical uncorrected, 2 – dynamically corrected;  $N_1 = 64$  samples/period,  $n = 5$  samples,  $m = 10$  samples

## 5. CONCLUSIONS

- Several methods of fast estimation of reactive and active power have been presented in the paper.
- Thanks to recognition of fault instant it is possible to take into account post fault samples of signals only.
- Such separation of pre fault and post fault samples allows to obtain unique, phase independent transients of estimation process i.e. before steady state of filters and estimator.
- These unique transients have each, any, reactive power estimator. Some of them apply orthogonal filters the other arbitrary FIR or IIR filters.
- These leads to the idea of dynamical correction using function which can be either calculated or obtained from digital simulation.
- Since the function depends of sampling frequency it is possible to keep in memory pre calculated or pre simulated values.
- Active power estimator can be realized using adequate delay of current signal to get phase shift of minus  $\pi/2$ .
- If noise level is small it is possible to get active or reactive power in two samples.
- In presence of noise it is possible to match responses of the filters to get given accuracy of estimation in given time.
- Development of estimators of the other protection criterion values and their performance tests will be realized soon.

REFERENCES

- [1] REBIZANT W., SZAFRAN J., WISZNIEWSKI A., *Digital Signal Processing in Power System Protection and Control*, Springer-Verlag London Limited, 2011, (Available in: <https://link.springer.com/book/10.1007/978-0-85729-802-7>).
- [2] ROSOŁOWSKI E., SZAFRAN J., *Fast Estimation of Protection Criterion Values Using Dynamical Correction*. Proc. of Eleventh PSCC, Avignon, August 30–September 3, 1993, Vol. II, pp. 805–811, (Available in: [https://psc-central.epfl.ch/repo/papers/1993/psc1993\\_99.pdf](https://psc-central.epfl.ch/repo/papers/1993/psc1993_99.pdf)).
- [3] ROSOŁOWSKI E., SZAFRAN J., *Dynamically corrected fast estimators of current and voltage magnitude*. IEE Proc.-Gener. Transm. Distrib., May 1995, Vol. 142. No. 3.
- [4] ROSOŁOWSKI E., *Digital Signal Processing in Power System Control*, Akademicka Oficyna Wydawnicza EXIT, Warszawa 2002 (in Polish), (Available in: <https://libra.ibuk.pl/book/147405>).
- [5] SZAFRAN J., WISZNIEWSKI A., *Mesurement and Decision Making in Digital Power System Control*, WNT, Warsaw 2001 (in Polish).
- [6] THORP J.S., PHADKE A.G., HOROWITZ S.H., BEEHLER J.E., *Limits to Impedance Relaying*, IEEE Trans. on PAS, Jan., Feb. 1979, Vol. PAS 98, No. 1, pp. 246–256.
- [7] UNGRAD H., WINKLER W., WISZNIEWSKI A., *Protection Techniques in Electrical Energy Systems*. Marcel Dekker, Inc., 1995.
- [8] WISZNIEWSKI A., *Digital high-speed calculation of the distorted signal fundamental component*, IEE Proc., January 1990, Vol. 137, Pt. C, No. 1, pp. 19–24.

